Multi-particle models of molecular diffusion for Lagrangian simulation coupled with LES for passive scalar mixing in compressible turbulence

Youming Tai[a], Tomoaki Watanabe[a,1,*], Koji Nagata[a]

[a]*Department of Aerospace Engineering, Nagoya University, Nagoya 464-8603, Japan*

Abstract

Lagrangian simulation coupled with large eddy simulation (LES) is studied for turbulent scalar mixing in compressible flows, where Lagrangian simulation solves advection-diffusion equations with computational particles. In Lagrangian simulation, a molecular diffusion term needs to be modeled with a so-called mixing model, which also requires modeling the dissipation rate of scalar fluctuations. The present study extends a particle-based subgrid-scale model for the scalar dissipation rate to compressible flows, and its validity in compressible turbulence is examined with direct numerical simulation databases of a temporally evolving turbulent planar jet with a jet Mach number of 0.6 or 1.6. A priori test confirms that the model can well predict the mean scalar dissipation rate in the subsonic and supersonic turbulent jets. The model hardly depends on the spatial distribution of the particles when the number of particles used in the model is about 12. However, the scalar dissipation rate tends to be overestimated by the model in regions with large dilatation fluctuations although such regions with strong compressibility ef-

*Corresponding author (+81-052-789-3279)
Email address: watanabe.tomoaki@c.nagoya-u.jp (Tomoaki Watanabe)

fects occupy only a small part of the flow. Lagrangian simulation coupled with LES of the turbulent jet is also performed with the scalar dissipation model combined with the mixing volume model. Lagrangian simulation with these models effectively predicts passive scalar statistics, such as averages, rms fluctuations, and turbulent fluxes, in the turbulent jet with both subsonic and supersonic jet velocities. The scalar dissipation model well predicts the coarse-grained scalar dissipation rate in Lagrangian simulation. The present results confirm that the mixing volume model combined with the the particle-based model of the scalar dissipation rate is useful in Lagrangian simulation coupled with LES, which is a promising approach for simulating high-speed turbulent reacting flows as reaction terms appear in Lagrangian simulation in a closed form.
Keywords: Turbulent mixing, Mixing model, Large eddy simulation, Turbulent jet, Compressible flows

1. Introduction

Chemical reaction in high-speed turbulent flows is a common phenomenon that is encountered in various engineering problems. Computational fluid dynamics (CFD) simulation is a valuable tool in the efficient development of engineering products. For instance, the CFD simulations with detailed chemical kinetics have been used for designing powertrain systems with fuel consumption and hazardous gas generation, which is often difficult to handle in experiments.[1,2,3] In recent decades, large eddy simulation (LES) has been extensively studied for industrial applications. LES solves governing equations for large-scale components of flow variables with coarse computational

grids while unresolved small-scale components are treated with subgrid-scale (SGS) models. Owing to significant advances in computational resources and numerical methods, recent LES can accurately predict large-scale characteristics of flows with a moderate computational cost. In turbulent reacting flows, molecular diffusion and reactions actively occur at small scales as turbulence inherently generates small-scale fluid motions. Therefore, the SGS models are crucial for LES of turbulent reacting flows. However, it is known that modeling SGS chemical source terms[4,5] has posed a formidable challenge since the number of existing chemical mechanisms is tremendous and the models often need to be optimized for a specific type of reactions.

LES is often combined with other models to avoid the modeling issues of the SGS chemical source terms. For example, conditional moment closure (CMC)[6] and filtered density function (FDF) model[7] have been used with LES, where LES solves the velocity field of a flow while CMC and FDF are used to solve equations of chemical concentration (or mass fraction). The FDF usually uses computational particles for solving governing equations, where chemical source terms appear in a closed form.[8,9] LES coupled with the FDF model has been applied to compressible flows.[7,10,11,12] Similarly, a particle-based solver of the transport equations of chemical concentration can be used with LES.[13,14] In Lagrangian simulation combined with LES, fluid particles are tracked with the velocity provided by LES. Each particle possesses scalar information, such as concentration, and the simulation calculates the Lagrangian evolution of scalars. In the case of chemical concentration, its evolution along each particle path is expressed with molecular diffusion and chemical source terms. Fully-Eulerian LES of turbulent reacting flows

requires models for SGS chemical source terms, which represent the effects of SGS fluctuations of species concentration. The advantage of Lagrangian simulation combined with LES is that the chemical source terms appear in a closed form.[15,16] However, Lagrangian simulation requires a model for molecular diffusion, which is often called a mixing model.[16] One of the commonly used mixing models is interaction exchange with mean (IEM) model,[17] which uses a relaxation process to mean concentration. Almost all mixing models have a parameter called a mixing timescale, which determines the decay rate of scalar fluctuations. Originally, the IEM model was developed for simulations based on Reynolds-averaged Navier-Stokes (RANS) equations, and the mixing timescale is defined with a scalar variance and its dissipation rate, which are also defined with Reynolds averages. The IEM model and similar mixing models developed in RANS have been applied with very little modification even for LES combined with Lagrangian simulation. Recently, the IEM model was extended to the mixing model in the framework of LES,[18] where relaxation to a local volume average approximates molecular diffusion. Here, the volume average works as a low-pass filter, and the mixing timescale is defined with an SGS scalar variance and its dissipation rate. As the model considers a mixing volume in which the relaxation process is applied, this LES version of the IEM model is called "mixing volume model (MVM)" in this study.

Accurate calculation of the mixing timescale τ is crucial for the mixing models. The definition of τ usually contains the scalar dissipation rate, which is defined with a local scalar gradient. Coarse-grained scalar dissipation rate appears in the definition of τ in the MVM developed for LES.[14] In general,

LES and Lagrangian simulation do not have a spatial resolution that is fine enough to directly calculate the scalar gradient. The scalar dissipation rate or its related quantity must be modeled for the application of the mixing models. In previous studies on Lagrangian simulation with mixing models, a constant timescale ratio between scalar and velocity fields is often assumed for calculating τ from the timescale of turbulence, which can be defined solely with the velocity field in LES.[13,19] Alternatively, the mixing timescale can also be calculated with the SGS models of filtered scalar dissipation rate applied in LES.[20,21,22] However, the mixing timescale depends on the length scale, which is generally different between particle distribution and computational grids. In this approach, the calculation of the mixing timescale for Lagrangian simulation requires an additional assumption for the scale dependence of the mixing timescale.[23,19] A direct approach is to model the coarse-grained scalar dissipation rate from the particle field. For this purpose, the SGS model of the filtered scalar dissipation rate developed for LES[21] has been recently extended to the particle-based model of the coarse-grained scalar dissipation rate.[24]

These recent developments of the models for molecular diffusion are limited for incompressible turbulent flows despite importance in practical applications to high-speed flows.[18,24] This paper presents an extension of the MVM and the coarse-grained scalar dissipation model to compressible flows. Unlike other existing models based on the timescale ratio between scalar and velocity fields, the models considered in this study estimate the mixing timescale without using adjustable parameters. One of the important differences between the classical IEM model and the MVM considered in this

study is in the definition of the mixing timescale. The MVM defines the mixing timescale such that the model provides the correct decay rate of local scalar variance while the classical IEM model concerns the decay of scalar variance defined with Reynolds averaged quantities. Therefore, the MVM is more appropriate in the application to LES than the IEM model. The main goal of this study is to evaluate these models extended to compressible flows by implementing them in Lagrangian simulation coupled with LES. As the primary interest is in the performance of the models related to molecular diffusion, LES and Lagrangian simulation are performed for a compressible turbulent planar jet with inert, passive scalar, which is often considered as a good approximation of concentration of dilute gas. However, Lagrangian simulation coupled with LES with the mixing model can easily be extended to simulations of turbulent reacting flows as already reported for incompressible flows[14,25]. The models are evaluated by comparing the results of LES and Lagrangian simulation with the DNS database.[26]

The paper is organized as follows. Sec. 2 describes LES and Lagrangian simulation, where the molecular diffusion term in Lagrangian simulation appears as an unclosed term. Sec. 3 presents the MVM for the molecular diffusion as well as the particle-based model of the coarse-grained scalar dissipation rate extended to compressible flows. The model for the coarse-grained scalar dissipation rate is tested with the DNS database in Sec. 4 while the results of LES and Lagrangian simulation with these models are discussed in Sec. 5. Finally, the conclusion is given in Sec. 6.

2. Lagrangian simulation of scalar mixing coupled with large eddy simulation

This section describes Lagrangian simulation coupled with LES for passive scalar mixing in a compressible flow. Here, we consider implicit LES, in which SGS terms are implicitly modeled by numerical schemes.[27] However, other SGS models can also be used in LES. LES solves governing equations for fluid density, velocity, and temperature on computational grids. The evolution of scalars (e.g., mass fractions and molar concentrations) is calculated in Lagrangian simulation, which is a combination of fluid-particle tracking and a mixing model. Particles used in Lagrangian simulation of scalar mixing have to be passive to the flow because the advection of scalars is represented by the particle movement.[28] Therefore, the interaction between particles and flow does not exist in Lagrangian simulation used for scalar mixing. Lagrangian simulation is conducted by interpolating flow variables in LES onto particle positions. If chemical reactions are also considered, the chemical source terms in Lagrangian simulation can easily be added without additional turbulence models on chemical source terms as the source terms appear in a closed form in Lagrangian simulation.[25]

Because the present study is devoted to investigating the models for molecular diffusion presented in this section, we only consider a single passive scalar φ without chemical reactions (e.g., dilute concentration of inert gas). However, the present method can easily be extended to a flow with multiple reactive scalars.[13,14] Because a passive scalar is considered, LES is performed independently from Lagrangian simulation (one-way coupled simulation). LES and Lagrangian simulation have to be two-way coupled if

the scalars in Lagrangian simulation are not passive to the flow (e.g., mass fractions of chemicals whose reactions cause significant heat release). In this case, a feedback scheme from Lagrangian simulation to LES is required as also used in previous studies.[29,30]. The formulation of the mixing model considered in this paper is independent of whether LES and Lagrangian simulation are one-way or two-way coupled. Therefore, the performance of the model is better evaluated for passive scalars (one-way coupled simulations) than for active scalars (two-way coupled simulations) since the feedback scheme used in two-way coupled simulations can be an additional source of errors. For this reason, the model is tested in one-way coupled simulation (passive scalar) in this study.

2.1. Implicit large eddy simulation

Navier-Stokes equations for compressible fluid (air) are used as governing equations. LES solves the equations for large-scale components of variables, which are defined with a low-pass filter. A low-pass filtered variable is denoted by $\overline{f}$ while a Favre-filtered variable is defined with density ρ as $\widetilde{f} = \overline{\rho f}/\overline{\rho}$.

The non-dimensional filtered Navier-Stokes equations can be written as

$$\frac{\partial \overline{\rho}}{\partial t} + \frac{\partial \overline{\rho}\widetilde{u}_j}{\partial x_j} = 0, \tag{1}$$

$$\frac{\partial \overline{\rho}\widetilde{u}_i}{\partial t} + \frac{\partial \overline{\rho}\widetilde{u}_i\widetilde{u}_j}{\partial x_j} = -\frac{\partial \overline{P}}{\partial x_i} + \frac{1}{Re}\frac{\partial \widetilde{\tau}_{ij}}{\partial x_j} + \beta(\overline{\rho}\widetilde{u}_i), \tag{2}$$

$$\begin{aligned}\frac{\partial \overline{\rho}\widetilde{T}}{\partial t} + \frac{\partial \overline{\rho}\widetilde{T}\widetilde{u}_j}{\partial x_j} = &-(\gamma-1)\overline{P}\frac{\partial \widetilde{u}_j}{\partial x_j} + \frac{\gamma}{RePr}\frac{\partial}{\partial x_j}\left(\widetilde{\mu}\frac{\partial \widetilde{T}}{\partial x_j}\right) \\ &+ \frac{\gamma-1}{Re}\widetilde{\tau}_{ij}\frac{\partial \widetilde{u}_i}{\partial x_j} + \beta(\overline{\rho}\widetilde{T}).\end{aligned} \tag{3}$$

The filtered viscous stress tensor $\widetilde{\tau}_{ij}$ is assumed to be given by

$$\widetilde{\tau}_{ij} = \widetilde{\mu}\left(\frac{\partial \widetilde{u}_i}{\partial x_j} + \frac{\partial \widetilde{u}_j}{\partial x_i} - \frac{2}{3}\delta_{ij}\frac{\partial \widetilde{u}_k}{\partial x_k}\right). \tag{4}$$

The equation of state for ideal gas is written as

$$\overline{P} = \overline{\rho}\widetilde{T}. \tag{5}$$

Here, x_i is the position vector, t is the time, u_i is the velocity vector, T is the temperature, P is the pressure, μ is the temperature-dependent viscosity coefficient, and $\gamma = c_p/c_v = 1.4$ is the specific heat ratio. Subscript indices $i, j = 1, 2, 3$ represent x, y, and z directions, respectively. A summation is taken over repeated indices in each term. β in Eqs. (2, 3) represents the contribution from unresolved scales, which have to be modeled by the SGS models. In implicit LES, β is implicitly modeled by artificial dissipation of numerical schemes or low-pass filters that take into account the dissipation in unresolved scales. The nondimensional variables f in the governing equations are related to their dimensional counterparts $\hat{f}$ by

$$x_i = \frac{\hat{x}_i}{l_r};\ u_i = \frac{\hat{u}_i}{u_r};\ \rho = \frac{\hat{\rho}}{\rho_r};\ t = \frac{\hat{t}u_r}{l_r};\ T = \frac{\hat{T}R}{u_r^2};\ \mu = \frac{\hat{\mu}}{\mu_r};\ P = \frac{\hat{P}}{\rho_r u_r^2}. \tag{6}$$

Here, $R = c_p - c_v = 287$ [J/(kg K)] is the gas constant, and the subscript r represents a reference quantity. Here, l_r, u_r, ρ_r, and μ_r are reference values of length, velocity, density, and viscosity coefficient, respectively. The definition of the reference quantities depends on problems. In the case of a planar jet considered below, the nozzle width, jet velocity, and density and viscosity coefficient of the jet fluid are used as the reference quantities. $Pr = \hat{\mu}c_p/\hat{k}$ is the Prandtl number that relates the thermal conductivity k to the viscosity coefficient μ. The Reynolds number Re is defined as $Re = \rho_r u_r l_r/\mu_r$.

2.2. Lagrangian simulation of passive scalar mixing

Lagrangian simulation is used to simulate the evolution of passive scalar φ, whose profile is represented by many computational particles. Hereafter, the number of particles is denoted by N_{P}. The position of particle n is denoted by $\mathbf{x}^{(n)}$ while the passive scalar φ evaluated at the particle position is represented by $\varphi^{(n)}$. The nondimensional governing equation for $\varphi = \hat{\varphi}/\varphi_r$ (φ_r: a reference scalar value) is written as

$$\frac{\partial \rho\varphi}{\partial t} + \frac{\partial \rho\varphi u_j}{\partial x_j} = \frac{1}{ScRe}\frac{\partial}{\partial x_j}\Big(\mu\frac{\partial \varphi}{\partial x_j}\Big), \tag{7}$$

where the Schmidt number is defined by $Sc = \hat{\mu}/(\hat{\rho}\hat{D})$ with the molecular diffusivity $\hat{D}$. If the equation is solved for a mass fraction, $\hat{\varphi}$ may denote the mass fraction with $\varphi_r = 1$ as the mass fraction is already non-dimensional. The Lagrangian description provides the governing equations of particles used in Lagrangian simulation coupled with LES,[14] which are written as

$$\frac{d\mathbf{x}^{(n)}}{dt} = \widetilde{\mathbf{u}}^{(n)}(t) = \widetilde{\mathbf{u}}(\mathbf{x}^{(n)}; t), \tag{8}$$

$$\frac{d\varphi^{(n)}}{dt} = \left[\frac{1}{ReSc\rho}\nabla\cdot(\mu\nabla\varphi)\right]^{(n)} = D_{\varphi}^{(n)}. \tag{9}$$

The particle movement is approximated with the resolved velocity interpolated from LES. The molecular diffusion term $D_{\varphi}^{(n)}$ in Eq. (9) cannot be directly evaluated from the particles because the particle field does not have the spatial resolution that is fine enough to calculate the local scalar gradient. The present paper applies the MVM combined with the particle-based coarse-grained scalar dissipation model to the molecular diffusion term.

Equation (8) neglects SGS velocity fluctuations, whose influences on the evolution of $\mathbf{x}^{(n)}$ and $\varphi^{(n)}$ are discussed here. The particle movement in

Eq. (8) is responsible for mean advection and turbulent diffusion, which are in general dominated by large-scale fluctuations. As LES resolves large-scale components of the velocity field, these effects are well captured by Eq. (8) even if the SGS fluctuations are neglected. Most mixing models used for molecular diffusion are based on the interaction among particles,[16] where the relative location among particles is important in the models. The Richardson's relative dispersion problem indicates that the relative location among fluid particles changes mostly by the eddies whose length scale is close to the distance among the particles.[31] Eddies with a size much larger or smaller than the particle distance advect particles without a significant change in the distance among the particles. Thus, as long as LES resolves the length scale close to the distance among the nearest particles, SGS velocity fluctuations have only a small influence on the relative location of particles. This is the case when the number of LES grids occupied by one particle is larger than 1. This is often called the sparse condition in hybrid LES and Lagrangian simulation.[32] The sparse condition is also desirable for reducing the computational cost. Lagrangian simulation coupled with LES in this study is performed under the sparse condition.

3. Models for molecular diffusion and coarse-grained scalar dissipation rate in compressible flows

3.1. Mixing volume model

The mixing volume model (MVM) for compressible flows[26] is used as a closure for the molecular diffusion term $D_{\varphi}^{(n)}$ in Eq. (9). The model is based on a volume average in a mixing volume, which is assigned for each

particle. The mixing volume of particle n is denoted by V_{M}^n. Shape and size of the mixing volume are arbitrary. Typically, after particles in the vicinity of particle n are chosen as mixing particles, V_{M}^n can be defined as the volume that contains the mixing particles. Here, the mixing volume is conceptually important in this model as the formation of the model is based on the similarity between the volume average represented with particles and a low-pass filter used in conventional LES. The present study assumes that at least 4 particles are contained in V_{M}^n. The volume average of f within V_{M}^n is denoted by $\langle f|V_{\mathrm{M}}^n\rangle$, which is approximately calculated as an ensemble average of particles within V_{M}^n:

$$\langle f|V_{\mathrm{M}}^n\rangle \equiv \frac{\sum_{m=1}^{N_{\mathrm{P}}} G_n(\boldsymbol{x}^{(m)}) f^{(m)}}{\sum_{m=1}^{N_{\mathrm{P}}} G_n(\boldsymbol{x}^{(m)})}, \tag{10}$$

$$G_n(\boldsymbol{x}^{(m)}) = \begin{cases} 1 & \text{If } \boldsymbol{x}^{(m)} \text{ is in mixing volume } V_{\mathrm{M}}^n \\ 0 & \text{otherwise} \end{cases}. \tag{11}$$

Here, the kernel function G_n acts as a box filter whose cutoff length is related to the mixing volume size. Fluctuations of a variable f from the volume average are defined as $f''^{(n)} = f^{(n)} - \langle f|V_{\mathrm{M}}^n\rangle$, which can be used to define the variance in the volume $\langle f''|V_{\mathrm{M}}^n\rangle$. The MVM approximates $D_\varphi^{(n)}$ as a process that relaxes $\varphi^{(n)}$ toward the volume average $\langle\varphi|V_{\mathrm{M}}^n\rangle$:

$$D_\varphi^{(n)} = \frac{1}{\tau_\varphi}\left(\langle\varphi|V_{\mathrm{M}}^n\rangle - \varphi^{(n)}\right), \tag{12}$$

$$\tau_\varphi = \frac{\langle\varphi''^2|V_{\mathrm{M}}^n\rangle}{\langle\varepsilon_\varphi|V_{\mathrm{M}}^n\rangle}. \tag{13}$$

Here, ε_φ is the scalar dissipation rate, and is expressed as $\varepsilon_\varphi = (\mu/\rho ReSc)\nabla\varphi\cdot\nabla\varphi$ in the MVM. $\langle\varepsilon_\varphi|V_{\mathrm{M}}^n\rangle$ cannot be directly calculated from the mixing particles, and has to be modeled with an additional model for the coarse-grained

scalar dissipation rate.

3.2. Particle-based model of the coarse-grained scalar dissipation rate

This section presents the particle-based model for $\langle \varepsilon_\varphi | V_{\rm M}^n \rangle$. As the volume average works as a low-pass filter, $\langle \varepsilon_\varphi | V_{\rm M}^n \rangle$ is considered as the coarse-grained scalar dissipation rate. The present model is obtained as an extension of the SGS model of filtered scalar dissipation rate[21] developed for LES of compressible turbulence.[24] The model approximates $\langle \varepsilon_\varphi | V_{\rm M}^n \rangle$ with the coarse-grained quantities $\langle f | V_{\rm M}^n \rangle$, which can be directly calculated from the variable $f^{(n)}$ on the mixing particles as below.

For convenience, an integer $\alpha_n = 1, ..., N_{\rm M}$ is introduced for referring to the mixing particles contained in $V_{\rm M}^n$, where the average can be written as $\langle f | V_{\rm M}^n \rangle = (1/N_{\rm M}) \sum_{\alpha_n=1}^{N_{\rm M}} f^{(\alpha_n)}$. Particle distribution in the volume $V_{\rm M}^n$ can be characterized by a volumetric tensor,[33] which is the 3×3 matrix defined by

$$R_{ij} = \langle r_i r_j | V_{\rm M}^n \rangle, \tag{14}$$

where $r_i^{(n)} = x_i^{(n)} - \langle x_i | V_{\rm M}^n \rangle$ is the particle position in relation to the center of the mixing particles. The coarse-grained gradient $\langle \partial f / \partial x_j | V_{\rm M}^n \rangle$ can be estimated from the mixing particles with the volumetric tensor by the following relation[34]:

$$\left\langle \frac{\partial f}{\partial x_j} | V_{\rm M}^n \right\rangle = \frac{1}{2N_{\rm M}^2} \sum_{\alpha_n=1}^{N_{\rm M}} \sum_{\beta_n=1}^{N_{\rm M}} \left(f^{(\alpha_n)} - f^{(\beta_n)} \right) \left({r_k}^{(\alpha_n)} - {r_k}^{(\beta_n)} \right) R_{kj}^{-1}, \tag{15}$$

where R_{ij}^{-1} is the inverse of the volumetric tensor, the summation is taken for the repeated index k, and the integers α_n and β_n denote $N_{\rm M}$ particles within

V_{M}^n. This estimation is based on a linear approximation of the gradient between two particles and least square estimation from all particle pairs within the volume.

If the number density of particles within a computational domain is high enough, the distance among the particles is close to the smallest scale of turbulence, and Eq. (15) yields a fully resolved gradient of f. However, computational cost limits the total number of particles within the computational domain, and $\langle \partial f/\partial x_j | V_{\mathrm{M}}^n \rangle$ only contains a contribution from scales greater than size of the mixing volume. In this study, we adapt the following model for the coarse-grained scalar dissipation rate $\langle \varepsilon_\varphi | V_{\mathrm{M}}^n \rangle$ in compressible turbulence:

$$\langle \varepsilon_\varphi | V_{\mathrm{M}}^n \rangle = C_{\varepsilon\varphi} \langle D | V_{\mathrm{M}}^n \rangle \left\langle \frac{\partial \varphi}{\partial x_j} | V_{\mathrm{M}}^n \right\rangle \left\langle \frac{\partial \varphi}{\partial x_j} | V_{\mathrm{M}}^n \right\rangle, \tag{16}$$

where the non-dimensional diffusivity coefficient at the particle position, $D^{(n)}$, is obtained by interpolating $D = \widetilde{\mu}/(\overline{\rho} ScRe)$ from LES. This formulation is derived from the SGS model for the filtered scalar dissipation rate in compressible flows.[21] The model parameter $C_{\varepsilon\varphi}$ indicates the ratio of dissipation rate from all length scales to that from scales greater than the size of the mixing volume. According to the original SGS model for LES,[21] $C_{\varepsilon\varphi}$ is dynamically estimated by integrating a model dissipation spectrum over the wavenumber k:

$$C_{\varepsilon\varphi} = \frac{\int_0^\infty k^2 E_\varphi(k) dk}{\int_0^\infty k^2 \hat{G}^2(k, L_{VT}) E_\varphi(k) dk}, \tag{17}$$

where $E_\varphi(k)$ is the model spectrum for passive scalar, and $\hat{G}$ is defined as

the spectral expression of the box filter used in the definition of $\langle f|V_{\rm M}^n\rangle$:

$$\hat{G}(k, L_{VT}) = \frac{\sin(kL_{VT}/2)}{kL_{VT}/2}. \tag{18}$$

The cutoff length L_{VT} is related to the particle distribution, which is well characterized by the volumetric tensor R_{ij}. The trace of R_{ij} is equal to the mean square distance between the particle position $x_i^{(\alpha_n)}$ and the center of the mixing particles $\langle x_i^{(\alpha_n)}|V_{\rm M}^n\rangle$. Therefore, L_{VT} is calculated as $L_{VT} = 2\sqrt{R_{11}+R_{22}+R_{33}}$. The present study uses the following model spectrum for scalar fluctuations in turbulence[21]:

$$E_\varphi(k) = Ak^{-5/3}\exp[-1.73(kL_\varphi)^{-4/3} - 2.25(k\eta_\varphi)^{4/3}], \tag{19}$$

where the integral scale of the scalar fluctuations L_φ and the Batchelor scale η_φ are estimated as

$$L_\varphi = 3\sqrt{k_r/(S_v)_{ij}(S_v)_{ij}}, \quad \eta_\varphi = 1.5(ScL_\varphi)^{1/4}\left(\frac{\sqrt{k_r}}{\langle D|V_{\rm M}^n\rangle}\right)^{-3/4}. \tag{20}$$

These length scale estimations are based on Re and Sc dependence of the Batchelor scale in fully-developed turbulence and an assumption that the integral scale of φ is close to that of velocity.[21] Here, $(S_v)_{ij} = 0.5(\langle\partial\widetilde{u}_i/\partial x_j|V_{\rm M}^n\rangle + \langle\partial\widetilde{u}_j/\partial x_i|V_{\rm M}^n\rangle)$ is the coarse-grained strain-rate tensor and $k_r = \langle\widetilde{u}_j^2|V_{\rm M}^n\rangle - \langle\widetilde{u}_j|V_{\rm M}^n\rangle^2$ is related to the kinetic energy in particle relative motions with respect to the mean motion of the mixing particles, and these quantities are calculated from the velocity $\widetilde{\boldsymbol{u}}^{(\alpha_n)}$ interpolated from LES. The constant A in the model spectrum does not affact $C_{\varepsilon\varphi}$ because A is canceled out in Eq. (17).

The MVM combined with the model for the coarse-grained dissipation rate provides a closure for the molecular diffusion term in Eq. (9), and $D_\varphi^{(n)}$

can be calculated from $\varphi^{(n)}$ and other variables directly interpolated from LES. Therefore, being combined with LES, Eqs. (8, 9) can be numerically solved with a large number of particles in order to simulate the passive scalar field.

4. A-priori test for the coarse-grained scalar dissipation model

4.1. DNS database of subsonic and supersonic turbulent planar jets

The MVM combined with the coarse-grained scalar dissipation model is evaluated in a priori test, which is based on the DNS database of temporally evolving turbulent planar jets. The details of the DNS can be found in our previous papers.[26,35] The temporal jet develops with time in a computational domain that is assumed to be periodic in the streamwise direction, and shares many important statistical properties with a spatially-evolving jet.[36] These temporally evolving turbulent free shear flows are often considered in fundamental studies of turbulence.[37,38] Further explanations of the temporally evolving planar jet can be found in other papers.[36,39] The streamwise, lateral, and spanwise directions are represented by $x_1 = x$, $x_2 = y$, and $x_3 = z$, respectively. $y = 0$ is defined as the center of the jet. The viscosity coefficient is given by Sutherland's law as a function of temperature. The initial jet velocity and width are denoted by U_J and H, respectively. The passive scalar φ is equal to φ_J and 0 inside and outside the initial jet. The initial pressure $P_0 = 1.013 \times 10^5$ [Pa] is uniform in the computational domain. The initial temperature $T_0 = 300$ [K] is also uniform except for edges of the jet, where the temperature profile is obtained from the Crocco–Busemann relation[40] for considering shear layers. The initial density profile

is given by the equation of state. Hereafter, the density corresponding to P_0 and T_0 is denoted by ρ_0, which is the initial density value in the jet. The reference quantities in Eq. (6) are $l_r = H$, $u_r = U_\mathrm{J}$, $\rho_r = \rho_0$, and $\mu_r = \mu(T_0)$ while the reference scalar value is $\varphi_r = \varphi_\mathrm{J}$. U_J and H can be determined by specifying the jet Reynolds number $Re_\mathrm{J} = \rho_0 U_\mathrm{J} H/\mu(T_0)$ and the jet Mach number $M_\mathrm{J} = U_\mathrm{J}/\sqrt{\gamma R T_0}$. The present study uses the DNS database with $(Re_\mathrm{J}, M_\mathrm{J}) = (14,000, 0.6)$ and $(14,000, 1.6)$. In the temporally evolving planar jets, the statistics depend on time and y, and averages $\langle f \rangle$ are taken in homogeneous (streamwise and spanwise) directions. The temporal planar jet is initialized with the nondimensional mean streamwise velocity profile given by

$$\langle u \rangle = \frac{1}{2} + \frac{1}{2}\tanh\left(\frac{1-2|y|}{4\theta_\mathrm{J}}\right), \tag{21}$$

where $\theta_\mathrm{J} = 0.03$ is the initial thickness of the shear layers at the edges of the jet, while mean velocity components in other directions are 0. Furthermore, velocity fluctuations are imposed onto the mean velocity profile for $|y| \leq 0.5$, where spatially-correlated artificial velocity fluctuations are generated by a diffusion process.[41] The initial scalar profile is given by

$$\varphi = \frac{1}{2} + \frac{1}{2}\tanh\left(\frac{1-2|y|}{4\theta_\mathrm{J}}\right) \tag{22}$$

without any fluctuations.

DNS was performed with the code based on a finite difference method, and details cn be found in previous papers,[26,35] where fundamental characteristics of the flow are also discussed in comparison with experiments and other DNS of turbulent planar jets. DNS with both $(Re_\mathrm{J}, M_\mathrm{J}) = (14,000, 0.6)$ and $(14,000, 1.6)$ was conducted with the computational domain with $(L_x, L_y, L_z) =$

Table 1: DNS database of temporal planar jets. M_{T} and η are taken from the jet centerline.

Re_{J}	M_{J}	M_{T}	b_φ	η
$14,000$	0.6	0.17	1.46	4.10×10^{-3}
$14,000$	1.6	0.47	1.27	4.55×10^{-3}

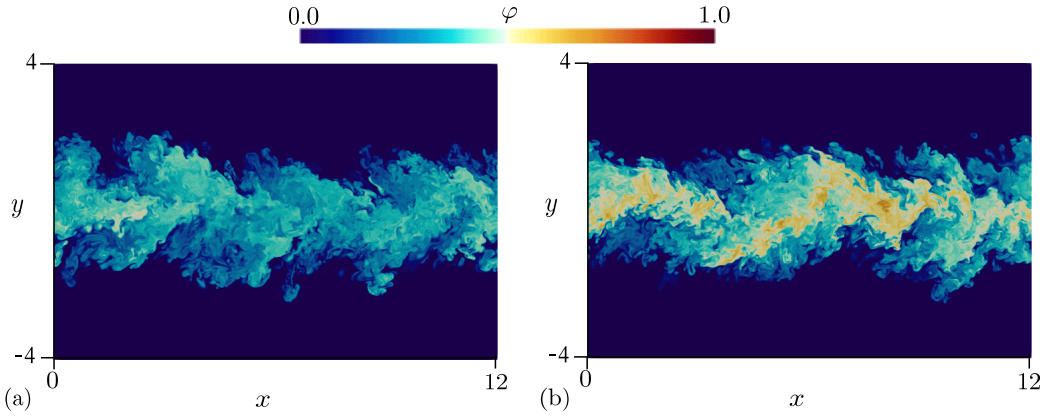

Figure 1: Passive scalar φ on a x-y plane at time $t = 26$ for (a) $M_{\mathrm{J}} = 0.6$ and (b) $M_{\mathrm{J}} = 1.6$.

$(12, 30, 6)$, which is represented by $(N_x \times N_y \times N_z) = (2200 \times 1400 \times 1100)$ grid points. The Prandtl and Schmidt numbers are $Pr = 0.71$ and $Sc = 1$, respectively. The computational grid size is smaller than 1.5 times Kolmogorov scale $\hat{\eta} = (\langle\hat{\mu}\rangle\langle\hat{\rho}\rangle)^{3/4}\langle\hat{\varepsilon}\rangle^{-1/4}$ in the turbulent jet, where $\hat{\varepsilon} = \hat{\tau}_{ij}\hat{S}_{ij}/\hat{\rho}$ is the kinetic energy dissipation rate and $\hat{S}_{ij}$ is the rate-of-strain tensor.

The turbulent jet develops with the time from the initial condition. In the present study, a priori test of the model is conducted at $t = 26$, by which turbulent the jet has fully developed. Fig. 1 visualizes φ on a x-y plane at $t = 26$, where small-scale scalar fluctuations due to turbulence

exist in the jet. φ is slightly smaller for $M_{\rm J} = 0.6$ than 1.6 because the jet development is delayed at high $M_{\rm J}$. Tab. 1 summarizes the turbulent Mach number $M_{\rm T} = \langle \hat{u}'_j \hat{u}'_j \rangle^{0.5} / \sqrt{\gamma R \langle \hat{T} \rangle}$, the jet half width based on the mean scalar profile b_φ, and the Kolmogorov scale η at $t = 26$. For $M_{\rm J} = 1.6$, the turbulent Mach number is high enough for compressibility effects to induce large density and temperature fluctuations in the turbulent jet, which may affect the mixing model by fluctuations of the diffusivity coefficient. The turbulent jet at $M_{\rm J} = 1.6$ also generates strong compression waves, which amplify local gradients of various quantities.[35]

4.2. A priori test of the coarse-grained scalar dissipation model

The coarse-grained scalar dissipation model in Sec. 3.2 is evaluated with the following procedures. One computational particle $\alpha_n = 1$ is placed on a DNS grid point while other $N_{\rm M} - 1$ particles are randomly placed within a spherical mixing volume with a radius $R_{\rm S}$ centered at particle 1. Important parameters of the model are the number of mixing particles $N_{\rm M}$ and the characteristic distance among particles, where the latter is related to $R_{\rm S}$. Variables in DNS are interpolated onto the particle positions with a tri-linear interpolation scheme. The error of the linear interpolation scheme is large when the grid spacing is not fine enough.[42] The grid spacing of the DNS database, 1.3η, is smaller than the criterion 2.1η, which is widely used in DNS studies.[43] As also assumed in DNS with particle tracking,[44] the linear interpolation with the fine grid spacing has a sufficient accuracy in a priori test of the model. It should also be noted that DNS of turbulent flows with the grid spacing of about 1.5η successfully observed a well-known Richardson scaling of two-particle dispersion for particles tracked with the

linear interpolation scheme.[45] Hereafter, the coarse-grained scalar dissipation rate $\langle \varepsilon_\varphi | V_{\mathrm{M}}^n \rangle$ is denoted by $[\varepsilon_\varphi]_{\mathrm{V}}$ for shortening the expression. From N_{M} particles, $[\varepsilon_\varphi]_{\mathrm{V}}$ is evaluated with the model given by Eq. (16). An exact value of $[\varepsilon_\varphi]_{\mathrm{V}}$ is calculated from $\varepsilon_\varphi^{(n)}$ at particle positions, which is obtained by interpolating ε_φ evaluated with an 8th-order central difference on the DNS grids. These procedures are repeated for different grid points where particle $\alpha_n = 1$ is placed. Statistics of $[\varepsilon_\varphi]_{\mathrm{V}}$ are calculated by taking averages on x-z planes. For each position of particle $\alpha_n = 1$, five sets of random numbers are used for determining the positions of other $N_{\mathrm{M}} - 1$ particles to improve statistical convergence. The model is evaluated for various parameter sets $(N_{\mathrm{M}}, R_{\mathrm{S}})$, and statistics of $[\varepsilon_\varphi]_{\mathrm{V}}$ are compared between the modeled value and its exact DNS value calculated with the central difference scheme.

4.3. Results and discussion

The average of the coarse-grained scalar dissipation rate $\langle [\varepsilon_\varphi]_{\mathrm{V}} \rangle$ is calculated for $[\varepsilon_\varphi]_{\mathrm{V}}$ obtained from the model and DNS. We define R_φ as the exact (DNS) value of $\langle [\varepsilon_\varphi]_{\mathrm{V}} \rangle$ divided by its value obtained by the model. Fig. 2 shows R_φ calculated on the jet centerline for a wide range of $(N_{\mathrm{M}}, R_{\mathrm{S}}/\eta)$. Profiles of R_φ are similar for both Mach numbers, and estimation of the mean coarse-grained scalar dissipation rate is hardly affected by compressibility of the flow. $R_\varphi \approx 1$ is required for the model to accurately estimate the coarse-grained scalar dissipation rate. Small R_φ for $N_{\mathrm{M}} < 8$ means that the coarse-grained scalar dissipation rate is overestimated by the model. Therefore, $[\varepsilon_\varphi]_{\mathrm{V}}$ in the model with $N_{\mathrm{M}} < 8$ is much larger than the exact DNS value for both Mach numbers. This tendency for small N_{M} is explained by the particle-based gradient estimation of Eq. (15), whose accuracy becomes

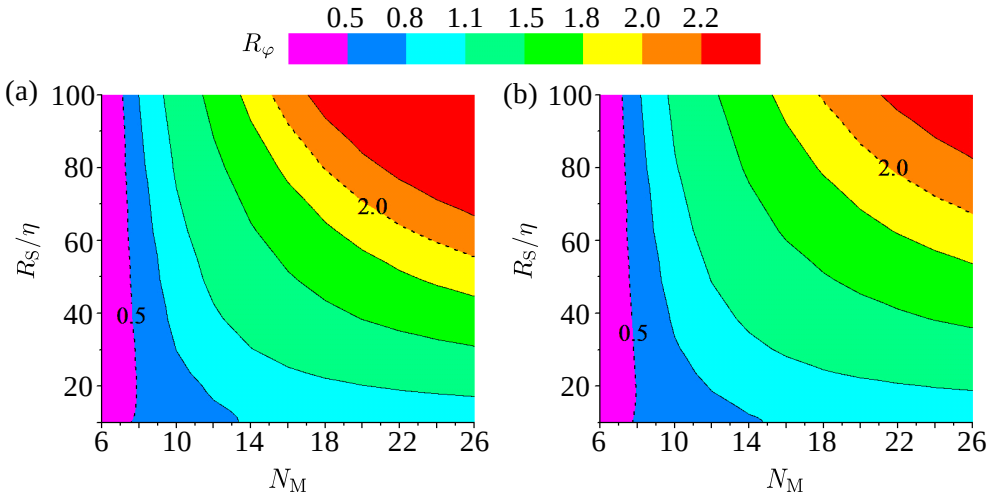

Figure 2: Contour map of R_φ plotted as a function of $(N_\mathrm{M}, R_\mathrm{S}/\eta)$ at $t = 26$ on the jet centerline: (a) $M_\mathrm{J} = 0.6$ and (b) $M_\mathrm{J} = 1.6$. Dash lines denote $R_\varphi = 0.5$ and 2.

worse as the number of particles decreases.[34] The coarse-grained gradient $\langle \partial\varphi/\partial x_i | V_\mathrm{M}^n \rangle$ yields the mean gradient $\langle \partial\varphi/\partial x_i \rangle$ if both N_M and R_S/η are very large. Here, $\langle \partial\varphi/\partial x_i \rangle$ is 0 on the jet centerline, and it does not represent the local scalar gradient at large scales anymore. Therefore, the coarse-grained dissipation rate tends to be underestimated when both R_S/η and N_M are large. One can find $R_\varphi \approx 1$ for a wide range of R_S/η when N_M is between 10 and 14 for both Mach numbers. This range of N_M is appropriate in Lagrangian simulation because the total number of the particles in Lagrangian simulation is limited by the computational cost, and the characteristic distance among mixing particles can be as large as 100η. Generally, a flow consists of regions with strong and weak compressibility effects. For example, the turbulent jet has a higher turbulent Mach number near the centerline than the edges of the jet. These regions can be treated with the

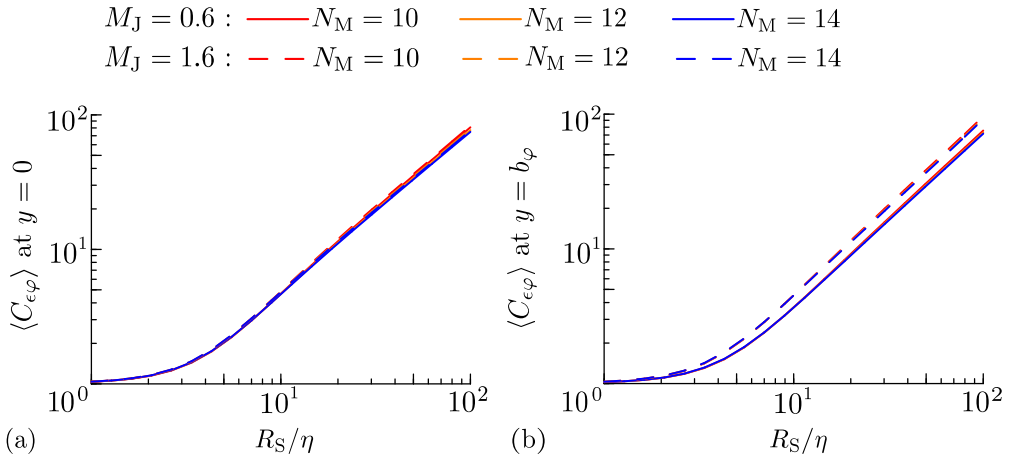

Figure 3: Averages of $C_{\varepsilon\varphi}$ plotted against R_S/η at (a) $y = 0$ and (b) $y = b_\varphi$.

present model without changing the parameters N_M and the size of the mixing volume because R_φ hardly depends on M_J.

The model dynamically calculates $C_{\varepsilon\varphi}$, whose average $\langle C_{\varepsilon\varphi} \rangle$ is calculated for a wide range of R_S/η with $N_M = 10$, 12, and 14. Fig. 3 shows $\langle C_{\varepsilon\varphi} \rangle$ as functions of R_S/η at $y = 0$ and b_φ. The definition of $C_{\varepsilon\varphi}$ indicates that $C_{\varepsilon\varphi}$ approaches 1 as R_S/η becomes small because $\langle \partial\varphi/\partial x_j | V_M^n \rangle$ with very small R_S/η provides the fully-resolved scalar gradient. At both lateral positions in Fig. 3, $\langle C_{\varepsilon\varphi} \rangle \approx 1$ for $R_S/\eta \leq 5$. The contribution of unresolved scales to the coarse-grained scalar dissipation rate becomes more significant as the length scale of the particle distribution increases, and therefore, $C_{\varepsilon\varphi}$ increases with R_S/η.

Fig. 4 compares the lateral profiles of the mean coarse-grained dissipation rate $\langle [\varepsilon_\varphi]_V \rangle$ between the model and DNS. Here, the results are shown only for $y \geq 0$ because the planar jet is symmetric for $y = 0$. Although $C_{\varepsilon\varphi}$ varies

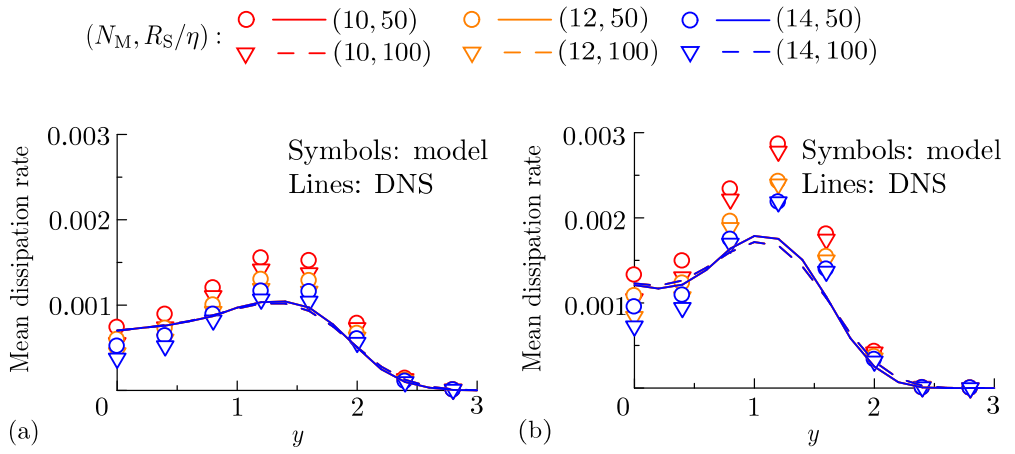

Figure 4: Lateral profiles of mean coarse-grained scalar dissipation rate $\langle [\varepsilon_\varphi]_V \rangle$ calculated by the central difference scheme in DNS (lines) and the model (symbols): (a) $M_J = 0.6$ and (b) $M_J = 1.6$ ($t = 26$).

between $O(10^0)$ and $O(10^2)$ depending on R_S, $\langle [\varepsilon_\varphi]_V \rangle$ in the model is close to the DNS results for various values of R_S/η, and the R_S dependence of the model is taken into account by the dynamical calculation of $C_{\varepsilon\varphi}$. $\langle [\varepsilon_\varphi]_V \rangle$ has a peak at $y \approx 1.5$ for $M_J = 0.6$ and $y \approx 1.0$ for $M_J = 1.6$. The peak is larger for $M_J = 1.6$ than $M_J = 0.6$ in DNS, and this tendency is well captured in the model although the peak tends to be overestimated by the model.

At the peak location of $\langle [\varepsilon_\varphi]_V \rangle$ in Fig. 4, difference between the model and DNS is more noticeable for higher Mach number. The deviation from DNS values in Fig. 4 is further examined with averages conditioned on root-mean-squared variance of the dilatation $\Theta = \partial u_i / \partial x_i$, which can be written as $\langle \Theta''^2 | V_M^n \rangle^{0.5} \equiv \sqrt{\langle \Theta^2 | V_M^n \rangle - \langle \Theta | V_M^n \rangle^2}$. $\langle \Theta''^2 | V_M^n \rangle^{0.5}$ is a measure of compress-

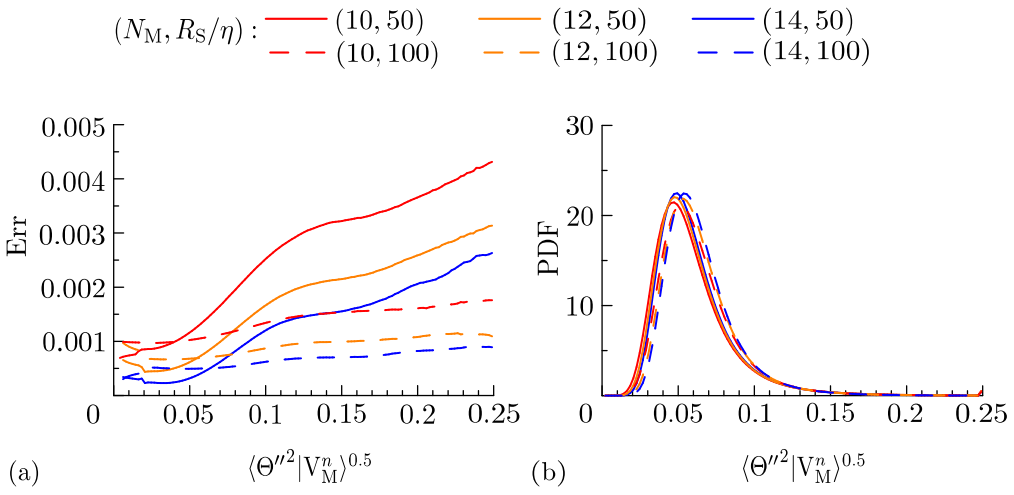

Figure 5: (a) Average of deviation of the model for $[\varepsilon_\varphi]_\mathrm{V}$ from DNS conditioned on $\langle\Theta''^2|V_\mathrm{M}^n\rangle^{0.5}$. (b) Probability density functions (PDFs) of $\langle\Theta''^2|V_\mathrm{M}^n\rangle^{0.5}$. Both results are obtained at $y = b_\varphi$ for $M_\mathrm{J} = 1.6$.

ibility in the region where the model is applied. Deviation of the model from the DNS value is defined as $([\varepsilon_\varphi]_\mathrm{V})^{(\mathrm{Model})} - ([\varepsilon_\varphi]_\mathrm{V})^{(\mathrm{DNS})}$, whose average conditioned on $\langle\Theta''^2|V_\mathrm{M}^n\rangle^{0.5}$ is denoted by Err. Positive Err means that the model overestimates the coarse-grained scalar dissipation rate. Fig. 5(a) plots Err against $\langle\Theta''^2|V_\mathrm{M}^n\rangle^{0.5}$ at $y = b_\varphi$ for $M_\mathrm{J} = 1.6$. Fig. 4(b) has already shown that the model overestimates the mean coarse gradient dissipation rate at this location. Err increases with $\langle\Theta''^2|V_\mathrm{M}^n\rangle^{0.5}$, and $[\varepsilon_\varphi]_\mathrm{V}$ in the model becomes larger than the DNS value in the region with large dilatation fluctuations. Fig. 5(b) shows probability density functions (PDFs) of $\langle\Theta''^2|V_\mathrm{M}^n\rangle^{0.5}$, which hardly depend on R_S/η and N_M. In Fig. 5(a), Err for $R_\mathrm{S} = 50\eta$ becomes large especially for $\langle\Theta''^2|V_\mathrm{M}^n\rangle^{1/2} \geq 0.1$. However, probability for $\langle\Theta''^2|V_\mathrm{M}^n\rangle^{0.5} \geq 0.1$ is very small, and the mean coarse-scalar dissipation rate is relatively in-

sensitive to regions with large $\langle \Theta''^2 | V_{\rm M}^n \rangle^{0.5}$, where the dissipation is locally overestimated. One of the possible reasons of this behavior is in estimation of $C_{\varepsilon\varphi}$, where the model spectrum, Eq. (19), does not take into account the compressibility effects on the spectral shape. However, as the turbulent Mach number increases, scalar gradient fluctuations tend to be more intermittent in space, and the spectral shape at high wavenumber can be influenced by the compressibility.[46] The model spectrum that incorporates the compressibility effects may improve the present model at high Mach numbers.

5. LES and Lagrangian simulation of temporally evolving compressible planar jets

5.1. Numerical schemes for LES and Lagrangian simulation

The MVM combined with the particle-based dissipation model is implemented in Lagrangian simulation coupled with LES of compressible turbulent flows. The performance of the models is assessed by applying LES and Lagrangian simulation to the temporally evolving planar jets considered in Sec. 4. The results of LES and Lagrangian simulation are compared with the DNS database used in Sec. 4. The comparisons with DNS are ideal for evaluation of the models because both simulations can be performed under the same boundary and initial conditions, which are difficult to match between simulations and experiments. For the same reason, comparisons between DNS and other numerical methods with mixing models have been reported in the existing literature.[47,48,49] The code used in LES and Lagrangian simulation is described here.

Implicit LES solves Eqs. (1-3) with a finite difference method based on

fully-explicit numerical schemes for temporal and spatial discretization, an implicit SGS model, and a shock-capturing filter. This code has been developed from the DNS code used in our previous studies on compressible turbulent boundary layers and planar jets.[26,50,35] Time integration of Euler terms, i.e., advection and pressure terms, is performed with a five-step, fourth-order Runge-Kutta scheme,[51] whereas the remaining terms arising from viscous effects and thermal conduction are temporally integrated by a first-order, forward Euler scheme for reducing the computational cost. These mixed Runge-Kutta and Euler schemes have also been used for DNS of turbulent round jets and turbulent boundary layers.[52] Statistics of turbulence obtained in these DNS studies were shown to agree well with results of experiments and other DNS. Spatial derivatives are calculated by the 8th-order central difference scheme except for regions near computational boundaries, where the derivatives are calculated with lower-order schemes presented in Wang et al.[52]

Low-pass filters used as the implicit SGS model are applied to $\overline{\rho}$, $\overline{\rho}\widetilde{u}_i$, and $\overline{\rho}\widetilde{T}$ at the end of each time step. Although the SGS term does not appear in Eq. (1), the filter is applied to $\overline{\rho}$ to avoid unphysical growth of density fluctuations caused by the central difference scheme.[52] An 11-point stencil selective filter[53] is applied in an interior region away from the boundaries except for periodic boundaries. Hereafter, three indices (i, j, k) represent an orthogonal grid point in x, y, and z directions, respectively, with $i = 1, ..., N_x$, $j = 1, ..., N_y$, and $k = 1, ..., N_z$. We denote a variable f at (i, j, k) by $f_{i,j,k}$.

The selective filter in the x direction, F_x, applied to $f_{i,j,k}$ is expressed as

$$F_x * f_{i,j,k} = f_{i,j,k} - \sum_{n=-5}^{5} d_n f_{i+n,j,k}, \tag{23}$$

with $d_0 = 0.215044884112$, $d_1 = -0.187772883589$, $d_2 = 0.123755948787$, $d_3 = -0.059227575576$, $d_4 = 0.018721609157$, and $d_5 = -0.002999540835$. The filters in the y and z directions, F_y and F_z, can also be written with the same values of d_n. When a grid point used in the filter is located outside the computational domain, the above filtering scheme cannot be used unless periodic boundary conditions are applied. The non-centered low-pass filters[54] are used for the regions near non-periodic boundaries, which correspond to the boundaries in the y direction in LES of the planar jet. These filters in the y direction applied at $j = 1, ..., 5$ are given by

$$\begin{aligned}
F_y * f_{i,1,k} &= f_{i,1,k} - 2^{-10}\big(f_{i,1,k} - 5f_{i,2,k} + 10f_{i,3,k} - 10f_{i,4,k} + 5f_{i,5,k} - f_{i,6,k}\big),\\
F_y * f_{i,2,k} &= f_{i,2,k} - 2^{-10}\big(-5f_{i,1,k} + 26f_{i,2,k} - 55f_{i,3,k} + 60f_{i,4,k} - 35f_{i,5,k} + 10f_{i,6,k} - f_{i,7,k}\big),\\
F_y * f_{i,3,k} &= f_{i,3,k} - 2^{-10}\big(10f_{i,1,k} - 55f_{i,2,k} + 126f_{i,3,k} - 155f_{i,4,k}\\
&\qquad + 110f_{i,5,k} - 45f_{i,6,k} + 10f_{i,7,k} - f_{i,8,k}\big),\\
F_y * f_{i,4,k} &= f_{i,4,k} - 2^{-10}\big(-10f_{i,1,k} + 60f_{i,2,k} - 155f_{i,3,k} + 226f_{i,4,k}\\
&\qquad - 205f_{i,5,k} + 120f_{i,6,k} - 45f_{i,7,k} + 10f_{i,8,k} - f_{i,9,k}\big),\\
F_y * f_{i,5,k} &= f_{i,5,k} - 2^{-10}\big(5f_{i,1,k} - 35f_{i,2,k} + 110f_{i,3,k} - 205f_{i,4,k} + 251f_{i,5,k}\\
&\qquad - 210f_{i,6,k} + 120f_{i,7,k} - 45f_{i,8,k} + 10f_{i,9,k} - f_{i,10,k}\big).
\end{aligned}$$

The filters applied at $j = N_y - 4, ..., N_y$ are expressed in the same way as these filters. The filters are repeatedly applied in three directions as $F_y * [F_z * (F_x * f)]$.

The shock-capturing filter[55] is also applied to $\overline{\rho}$, $\overline{\rho}\widetilde{u}_i$, and $\overline{\rho}\widetilde{T}$ to prevent numerical instabilities due to Gibbs oscillations. The shock-capturing filter in the x direction, $F_x^{(S)}$, is expressed as

$$\begin{aligned} F_x^{(S)} * f_{i,j,k} = f_{i,j,k} - \Big[&- 0.5 \left(\sigma^{(x)}_{i-1,j,k} + \sigma^{(x)}_{i,j,k}\right) \Big(-d_1^{(S)} f_{i-2,j,k} + d_2^{(S)} f_{i-1,j,k} \\ &\qquad - d_2^{(S)} f_{i,j,k} + d_1^{(S)} f_{i+1,j,k}\Big) \\ &+ 0.5 \left(\sigma^{(x)}_{i,j,k} + \sigma^{(x)}_{i+1,j,k}\right) \Big(-d_1^{(S)} f_{i-1,j,k} + d_2^{(S)} f_{i,j,k} \\ &\qquad - d_2^{(S)} f_{i+1,j,k} + d_1^{(S)} f_{i+2,j,k}\Big)\Big], \end{aligned} \tag{24}$$

with $d_1^{(S)} = 0.039617$ and $d_2^{(S)} = 0.210383$. The filter strength is adjusted by $\sigma^{(x)}$, which is given by

$$\sigma^{(x)} = \frac{1}{2}\left(1 - \frac{r_m}{r^{(x)}} + \left|1 - \frac{r_m}{r^{(x)}}\right|\right). \tag{25}$$

Here, r_m is a threshold parameter of the filter, and $r^{(x)}$ is a measure of the shock wave strength. The shock wave strength is given by dilatation $\Theta = \partial \overline{u}_j / \partial x_j$, which is used to calculate $r^{(x)}$. Here, $r^{(x)}$ is determined by the high-wavenumber component of dilatation $D_{i,j,k} = (-\Theta_{i-1,j,k} + 2\Theta_{i,j,k} - \Theta_{i+1,j,k})/4$ and the speed of sound $c_{i,j,k} = \sqrt{\gamma \overline{P}_{i,j,k}/\overline{\rho}_{i,j,k}}$ at each grid point[55]:

$$r^{(x)}_{i,j,k} = \frac{0.5\left[(D_{i,j,k} - D_{i+1,j,k})^2 + (D_{i,j,k} - D_{i-1,j,k})^2\right]}{c^2_{i,j,k}/(\Delta_x)^2_{i,j,k}} + 10^{-16}, \tag{26}$$

where Δ_x is the grid spacing in the x direction. With $\sigma^{(x)}$ given by Eq. (25), the shock-capturing filter efficiently dumps fluctuations in the regions with strong discontinuity. The shock-capturing filter is subsequently applied in three directions as $F_y^{(S)} * [F_z^{(S)} * (F_x^{(S)} * f)]$ after the low-pass filters used as the implicit SGS model are applied. The constant threshold parameter r_m is

important in discriminating between turbulent fluctuations and Gibbs oscillations. An appropriate value of r_m can be determined from r_m-dependence of simulations as suggested in a previous study on implicit LES.[56] We have performed implicit LES of the turbulent jet with various values of r_m between 10^{-6} and 10^{1}. It has been confirmed that root-mean-squared (rms) velocity fluctuations in the jet do not depend on r_m between 10^{-3} and 10^{0}. For $r_m \geq 10^{1}$, the shock-capturing filter fails to suppress Gibbs oscillations, and the simulation stops due to numerical instability for the planar jet at $M_{\mathrm{J}} = 1.6$. On the other hand, the shock-capturing filter with $r_m \leq 10^{-3}$ causes an artificial decay of rms velocity fluctuations in the jet. Therefore, we use $r_m = 1$ in all simulations presented in this paper.

The temporally evolving planar jet is periodic in the streamwise and spanwise directions, for which periodic boundary conditions are applied. Subsonic outflow boundary conditions of Navier-Stokes characteristic boundary conditions (NSCBC)[51] are used at the boundaries in the y direction. Furthermore, the regions of $|y| > 7$ are treated as sponge zones, where the second-order low-pass filter[57] is applied to suppress pressure waves toward the boundaries. These boundary conditions are the same as in the DNS of the temporally evolving planar jet.[35] The grids are uniform in x and z directions, and the grid points in the y direction are determined by a mapping function based on a hyperbolic tangent function[26] that yields small grid spacing near the jet centerline.

In Lagrangian simulation, initial particle positions $\mathbf{x}^{(n)}$ are randomly determined while initial scalar values $\varphi^{(n)}$ are calculated from the prescribed initial condition of $\varphi(\mathbf{x}; t = 0)$ given by Eq. (22) as $\varphi^{(n)}(t = 0) = \varphi(\mathbf{x}^{(n)}; t = 0)$.

At each time step, variables in LES are interpolated on the particle positions with the tri-linear interpolation scheme. $\mathbf{x}^{(n)}$ and $\varphi^{(n)}$ change with time according Eqs. (8) and (9), respectively. Here, Eq. (8) is integrated with the 1st-order Euler scheme as $\mathbf{x}^{(n)}(t+\Delta t) = \mathbf{x}^{(n)}(t) + \widetilde{\mathbf{u}}^{(n)}(t)\Delta t$. The molecular diffusion term $D_\varphi^{(n)}$ is modeled by the MVM combined with the model for the coarse-grained scalar dissipation rate. The computational domain is divided into many rectangular subdomains that contain about $10N_\mathrm{M}$ particles. Here, N_M is treated as a computational parameter, and the number of the subdomain is determined from N_M, the total number of particles N_P, and the computational domain size. For particle n, the distance to nearby particles within the same subdomain is calculated to select $N_\mathrm{M}-1$ nearest particles as the mixing particles. The volume average $\langle f|V_\mathrm{M}^{(n)}\rangle$ is evaluated by averages of N_M particles. For particle n, the MVM changes φ for all mixing particles ($\alpha_n = 1, ..., N_\mathrm{M}$) by

$$\varphi^{(\alpha_n)}(t+\Delta t) = \begin{cases} \varphi^{(\alpha_n)}(t) + \dfrac{\Delta t}{N_\mathrm{M}\tau_\varphi}\left(\langle\varphi|V_\mathrm{M}^n\rangle - \varphi^{(\alpha_n)}\right) & \text{for } \Delta t < \tau_\varphi N_\mathrm{M} \\ \langle\varphi|V_\mathrm{M}^n\rangle & \text{for } \Delta t \geq \tau_\varphi N_\mathrm{M} \end{cases}. \tag{27}$$

This procedure is repeated for all particles $n = 1, ..., N_\mathrm{P}$. It should be noted that in the present implementation of the MVM, one particle can be involved in more than one mixing volume, and participates N_M mixing events on average in each time step. This influence of multiple mixing events is incorporated by replacing τ_φ by $N_\mathrm{M}\tau_\varphi$ from the original MVM. The MVM assumes that the time increment Δt in simulations is smaller than the timescale of mixing $N_\mathrm{M}\tau_\varphi$. This assumption is usually valid in the simulations because Δt is smaller than characteristic timescales of fluid motions and speed of sound.

Table 2: Computational parameters in LES and Lagrangian simulation of temporally evolving planar jets. η is calculated on the jet centerline at $t = 26$ in DNS.

Case	M_{J}	N_{P}	N_{M}	R_{MV}/η	T_{C}
1	0.6	$12,000$	8	120	1.00
2	0.6	$18,000$	12	120	1.01
3	0.6	$30,000$	12	100	1.04
4	0.6	$60,000$	12	80	1.13
5	0.6	$30,000$	20	120	1.07
6	1.6	$12,000$	8	110	1.00
7	1.6	$18,000$	12	110	1.01
8	1.6	$30,000$	12	90	1.04
9	1.6	$60,000$	12	70	1.13
10	1.6	$30,000$	20	110	1.07

However, τ_φ can be extremely small if N_{M} particles appear at almost same locations. The mixing in V_{M}^n completes within the time interval Δt if Δt is larger than $N_{\mathrm{M}}\tau_\varphi$. Therefore, in the case of $\Delta t \geq N_{\mathrm{M}}\tau_\varphi$, scalar values of the particles are simply replaced by the mean value $\langle\varphi|V_{\mathrm{M}}^n\rangle$ in Eq. (27), which is an equilibrium state of the MVM.

5.2. Computational parameters

LES coupled with Lagrangian simulation is performed for the temporally evolving planar jet with a rectangular computational domain with the size of $(L_x, L_y, L_z) = (12, 30, 6)$, which is nondimensionalized by the initial jet width H. LES should resolve large-scale fluctuations of turbulence. The

characteristic length scale of large-scale flow structures is different between the transitional and fully-developed regimes of the planar jet. Initially, the shear instability causes turbulent transition at the edges of the planar jet. The roller vortices arising from the instability are the typical large-scale structures in the transitional regime.[58] The size of the roller vortices is of the order of the initial shear layer thickness $\theta_{\mathrm{J}} = 0.03H$. The length scale of large-scale velocity fluctuations in the fully-developed turbulent jet is the width of the jet, which is of the order of the initial jet width H and is larger than the size of the roller vortices. Therefore, the grid size in LES is determined based on the size of large-scale structures in the transitional regime. LES coupled with Lagrangian simulation uses $(N_x, N_y, N_z) = (480, 300, 240)$ grid points in each direction. The grid dependence of LES is checked for $(N_x, N_y, N_z) = (360, 300, 180)$. The grid size in the x and z directions is $0.025H$ for the fine grid and $0.033H$ for the coarse grid, while the grid spacing in the y direction is $0.025H$ for both grids. These grid sizes are comparable to previous LES studies of a planar jet at $Re_{\mathrm{J}} = 70000$ and 60000,[24,40] and small enough to resolve the initial roller vortices at the edge of the planar jet.

As initial conditions, N_{P} computational particles are randomly placed within the region of $|y| < 4$ because the turbulent jet does not reach $|y| > 3$, where $\varphi = 0$ is constant during the simulation. The jet Reynolds number is $Re_{\mathrm{J}} = 14,000$ while the jet Mach number is $M_{\mathrm{J}} = 0.6$ or 1.6. Lagrangian simulation coupled with LES is performed with five parameter sets of $(N_{\mathrm{M}}, N_{\mathrm{P}})$ for each value of M_{J} as summarized in Tab. 2. The characteristic length of the mixing volume can be defined as $R_{\mathrm{MV}} = (3N_{\mathrm{M}}/4\pi\rho_{\mathrm{P}})^{1/3}$, where $\rho_{\mathrm{P}} = N_{\mathrm{P}}/(L_x \times 8 \times L_z)$ is the number density of particles. R_{MV} depends on

$(N_{\mathrm{M}}, N_{\mathrm{P}})$ in the present simulations. Cases 1, 2, and 5 are performed with $R_{\mathrm{MV}}/\eta = 120$ with different N_{M} while cases 2, 3, and 4 use $N_{\mathrm{M}} = 12$ and different R_{MV}/η. These parameters are chosen for assessing influences of N_{M} and R_{MV}. The parameters in cases 6-10 for $M_{\mathrm{J}} = 1.6$ are also chosen in the same way.

Statistics in Lagrangian simulation are calculated by taking ensemble averages of particles. The temporally evolving planar jet is statistically homogeneous in x and z directions, and the averages of the particles located at similar y are taken at each time step. Here, y coordinate between $-4 \leq L_y \leq 4$ is divided into 100 regions, and the particles located in each region are used as statistical samples there. This method is widely used to calculate the statistics in Lagrangian simulation of scalar mixing.[16] LES coupled with Lagrangian simulation for each case is repeatedly conducted with 10 sets of random numbers that determine the initial particle positions. The ensemble averages of the 10 simulations are also taken for improving statistical convergence. The statistics obtained in LES coupled with Lagrangian simulation are compared with the DNS database used in Sec. 4.

The computational time per one time step T_{C} is measured for each case as summarized in Tab. 2, where T_{C} is normalized so that the time is equal to 1 in case 1. The computational time of Lagrangian simulation coupled with LES slightly increases with N_{M} and N_{P}. The computational time spent for Lagrangian simulation increases with N_{P} because the governing equations for particles are solved for N_P times in each time step. As described above, the mixing particles are selected based on the distance between particles. The distance from one particle n is calculated for about $10N_{\mathrm{M}}$ particles that are

located in the same subdomain used to choose the mixing particles. Therefore, the computational time for the MVM increases with N_{M}. However, the total computational time of Lagrangian simulation and LES, T_{C}, weakly depends on N_{M} and N_{P} because LES consumes more computational time than Lagrangian simulation. The total memory size required to store the main variables is the sum of memory sizes in LES and Lagrangian simulation. The memory required in Lagrangian simulation is determined by the number of particles N_P in Lagrangian simulation. As the number of particles is smaller than the number of grid points, the order of the total memory size is determined by the number of the grid points in LES rather than the number of particles.

5.3. Results and discussions

LES results are compared with the DNS database. Figure 6 compares the lateral profile of the mean streamwise velocity between DNS and LES with fine and coarse grids. The mean velocity at each time has a peak on the jet centerline ($y = 0$). The profile is flattened with time as the streamwise momentum is transferred outward from the center of the jet. The mean velocity at $y = 0$ decays with time. The decay is slower for $M_{\mathrm{J}} = 1.6$ than 0.6. This is related to the delay of the jet development due to strong compressibility as the turbulent diffusion is suppressed for a high Mach number.[59] This compressibility effect on the jet development is well predicted by LES. The mean velocity profile in LES agrees well with DNS for both grid settings. Figure 7 compares rms fluctuations of streamwise velocity between DNS and LES. Here, rms fluctuations of f are defined as $[f]_{\mathrm{rms}} = \sqrt{\langle f^2 \rangle - \langle f \rangle^2}$. At $t = 6$, the rms velocity fluctuations have a peak

at $y \approx 0.6$, where the initial turbulent shear layers develop near the edge of the jet. In late time, the rms velocity fluctuations weakly depend on y for $|y| \lesssim 1.2$ as also found in a fully developed turbulent planar jet.[60] Figure 8 shows energy spectra of streamwise and lateral velocity fluctuations at $t = 12$ at the center of the jet with $M_{\rm J} = 0.6$. The spectra are calculated with Fourier transform in the x direction. For both streamwise and lateral velocity components, the spectra at large scales are consistent between LES and DNS. The spectrum of lateral velocity has a peak at $k_x \approx 2$, which is caused by flapping motions of the planar jet as also observed in experiments.[61,62] The spectra in LES become smaller than in DNS for $k_x \gtrsim 60$ and $k_x \gtrsim 50$ for the fine grid and coarse grid, respectively, and small-scale fluctuations are not resolved in LES. The length scale of the smallest turbulent motions is the Kolmogorov scale, which increases with time in the planar jet. Therefore, LES has relatively better resolution in late time, while the range of unresolved scales becomes wider in earlier time. However, the grid is fine enough to capture large-scale fluctuations, which have a dominant contribution to the rms velocity fluctuations. Therefore, LES successfully predicts the profile of rms velocity fluctuations in Fig. 7(b).

Fig. 9 compares the lateral profiles of mean values and rms fluctuations of density and temperature at $t = 26$. In Figs. 9(a) and (c), mean density and temperature are lower and higher, respectively, in the jet compared with the outside. The density decrease and temperature increase in the jet are more significant at higher $M_{\rm J}$. This tendency can also be seen in LES although the change of the mean density and temperature is underestimated. Figs. 9(b) and (d) shows that large fluctuations of density and temperature

are induced in the jet at $M_{\rm J} = 1.6$. Mach number dependence of the rms fluctuations is generally predicted well by LES although LES slightly underestimates rms temperature fluctuations. In Lagrangian simulation, the temperature and density in LES are interpolated onto the particle positions, and the diffusivity coefficient at the particle positions is calculated as $D^{(n)} = \widetilde{\mu}(\widetilde{T}^{(n)})/(\overline{\rho}^{(n)} ScRe)$. The mean temperature and density at $y = 0$ for $M_{\rm J} = 1.6$ provide the nondimensional diffusivity coefficient $D = 8.5 \times 10^{-5}$ in the DNS and $D = 8.0 \times 10^{-5}$ in LES. Therefore, the difference in D between LES and DNS is very small and is expected to be negligible in the mixing model used in Lagrangian simulation.

Fig. 10 compares the lateral mean scalar profiles $\langle\varphi\rangle$ between Lagrangian simulation and DNS. For higher $M_{\rm J}$, $\langle\varphi\rangle$ near the centerline has larger values while the lateral extension of the jet with $\langle\varphi\rangle > 0$ is narrower. The Mach number dependence of the mean scalar profile is similar between Lagrangian simulation and DNS. As also found for the mean velocity in Fig. 9(a), the Mach number dependence is due to the suppression of the turbulent diffusion by the compressibility. In the turbulent jet, the turbulent diffusion in the lateral direction dominates the transport equation of $\langle\varphi\rangle$ while the molecular diffusion hardly contributes to the mean scalar transport unless the Reynolds number is very low. Therefore, the mixing model and its related parameters do not affect the mean scalar profile, whose development is strongly depends on the particle velocity calculated in LES.

The lateral profiles of rms scalar fluctuations $[\varphi]_{\rm rms}$ are compared in Fig. 11. Unlike in the mean scalar transport equation, the molecular diffusion significantly contributes to the transport equation of the scalar vari-

ance $[\varphi]^2_{\rm rms}$ by the dissipation, which is treated by the MVM in Lagrangian simulation. The dissipation rate in Lagrangian simulation is controlled by the model for the coarse-grained scalar dissipation rate. In Figs. 11 (a) and (b), Lagrangian simulation with constant $R_{\rm MV}$ is compared for different $N_{\rm M}$. In a priori test, the modeled coarse-grained scalar dissipation rate tends to be small as $N_{\rm M}$ increases in Fig. 4. Consistently, the rms scalar fluctuations in Lagrangian simulation become large with $N_{\rm M}$. In cases 2 and 7 with $N_{\rm M} = 12$, the rms scalar fluctuations are well predicted by Lagrangian simulation, and the models work well for $N_{\rm M} \approx 12$ in Lagrangian simulation as also confirmed in a priori test. Figs. 11(c) and (d) show the rms scalar fluctuations obtained in Lagrangian simulation with $N_{\rm M} = 12$ for different $R_{\rm MV}$, where the results of Lagrangian simulation hardly depend on $R_{\rm MV}$ at both Mach numbers. A priori test in Fig. 2 also confirms that the model for the coarse-grained scalar dissipation rate hardly depends on $R_{\rm MV}$ for $N_{\rm M} = 12$. $N_{\rm M} = 12$ can be considered as a robust parameter, which can be used for subsonic and supersonic flows.

A relative difference of a statistical quantity f between DNS and Lagrangian simulation is defined as $|f_{\rm DNS} - f_{\rm LS}|/f_{\rm DNS}$, where $f_{\rm DNS}(y)$ and $f_{\rm LS}(y)$ are values of f in DNS and Lagrangian simulation, respectively. The mean difference can be evaluated with the integral as $\delta_f = (1/L_\delta)\int_0^{L_\delta}(|f_{\rm DNS} - f_{\rm LS}|/f_{\rm DNS})dy$, which is the spatial average of the relative difference. We evaluate δ_f with $L_\delta = 2.5$ and 2.0 for $M_{\rm J} = 0.6$ and 1.6, respectively, as the mean scalar is almost 0 outside these locations. At $t = 26$, we obtain $\delta_{\langle\varphi\rangle} = 0.105$ and $\delta_{[\varphi]_{\rm rms}} = 0.103$ for case 2 ($M_{\rm J} = 0.6$) and $\delta_{\langle\varphi\rangle} = 0.159$ and $\delta_{[\varphi]_{\rm rms}} = 0.132$ for case 7 ($M_{\rm J} = 1.6$), and the averaged relative errors are

about 10%. Nonetheless, the overall features of the lateral profiles of these statistics are well captured in Lagrangian simulation.

Fig. 12 shows the lateral profiles of the turbulent scalar flux in the y direction, $\langle \rho u_y' \varphi' \rangle$. Their profiles are predicted well by Lagrangian simulation. Accurate prediction of the turbulent flux is related to the good agreement of the mean scalar profile between DNS and Lagrangian simulation. It should be noted that the velocity that approximates particle motions in Eq. (8) is obtained from LES, and does not contain a contribution from unresolved scales. However, the comparison of $\langle \rho u_y' \varphi' \rangle$ between the DNS and Lagrangian simulation confirms that velocity fluctuations in the unresolved small scales hardly affect the turbulent transport of φ.

The coarse-grained scalar dissipation rate $[\varepsilon_\varphi]_{\rm V}$ is calculated for each particle in Lagrangian simulation. Fig. 13 compares the mean coarse-grained scalar dissipation rate $\langle [\varepsilon_\varphi]_{\rm V} \rangle$ in Lagrangian simulation with $N_{\rm M} = 12$ with the mean scalar dissipation rate $\langle \varepsilon_\varphi \rangle$ in DNS. $[\varepsilon_\varphi]_{\rm V}$ is the coarse-grained dissipation rate within the mixing volume, whose characteristic length, $R_{\rm MV}$, is about $0.2b_\varphi$-$0.4b_\varphi$ and is still smaller than the jet halfwidth b_φ. On the other hand, the length scale of the distribution of $\langle \varepsilon_\varphi \rangle$ is characterized by b_φ. Therefore, we can expect that $\langle [\varepsilon_\varphi]_{\rm V} \rangle$ and $\langle \varepsilon_\varphi \rangle$ have similar profiles because the local volume average within the mixing volume does not smear out the lateral mean profile of ε_φ. In Fig. 13, $\langle [\varepsilon_\varphi]_{\rm V} \rangle$ and $\langle \varepsilon_\varphi \rangle$ are close to each other at both Mach numbers, and $[\varepsilon_\varphi]_{\rm V}$ is accurately calculated with the particle model in Lagrangian simulation. As expected from a priori test, $\langle [\varepsilon_\varphi]_{\rm V} \rangle$ hardly changes with $R_{\rm MV}$ at $N_{\rm M} = 12$ even when the model is used in Lagrangian simulation.

Fig. 14 compares the PDF of φ at $y = 0$ and b_φ between DNS and Lagrangian simulation at $M_\mathrm{J} = 0.6$ while the PDF at $M_\mathrm{J} = 1.6$ are shown in Fig. 15. If the molecular diffusion effect modeled by the MVM is excluded from Lagrangian simulation, the particles move in the physical space without changing scalar values. Considering that the shape of the PDF is related to the evolution of $\varphi^{(n)}$ due to the MVM, it can be concluded that Lagrangian simulation with the MVM predicts fairly well the PDF on the centerline. However, the PDF at $y = b_\varphi$ in Lagrangian simulation does not have a large peak at $\varphi = 0$. The large peak at $\varphi = 0$ is due to the intermittent behavior of the turbulent jet, where the turbulent jet region with $\varphi > 0$ appears together with the external non-turbulent region with $\varphi = 0$. The second peak of the PDF for $\varphi \approx 0.3$ is associated with the scalar value that appears the most frequently inside the turbulent jet. An interfacial layer between the turbulent and non-turbulent regions is called a turbulent/non-turbulent interfacial (TNTI) layer, which has a small thickness about 10 times Kolmogorov scales in the compressible planar jet[35] and mixing layer.[63] Lagrangian simulation uses the MVM with $R_\mathrm{MV} \approx 100\eta$, which cannot accurately calculate the molecular diffusion near the TNTI layer. Comparing cases 2 and 4 in Fig. 14 or cases 7 and 9 in Fig. 15, one can find that the PDF at $\varphi = 0$ tends to be larger for small R_MV, and a smaller mixing volume in the MVM results in more accurate prediction of the PDF.

Finally, Fig. 16 compares the PDF of $[\varepsilon_\varphi]_\mathrm{V}$ for $N_\mathrm{M} = 12$ between Lagrangian simulation and DNS for $M_\mathrm{J} = 1.6$. Here, exact values of $[\varepsilon_\varphi]_\mathrm{V}$ is obtained from the instantaneous profile of ε_φ in DNS with the following method. N_P particles are randomly placed in the computational domain.

Then, ε_φ calculated with the 8th-order central difference scheme is interpolated onto the particle positions. The ensemble average of ε_φ among N_M particles is taken within the mixing volume to evaluate the exact value $[\varepsilon_\varphi]_\mathrm{V}$ with the same $R_{\mathrm{M}V}$ as in Lagrangian simulation. In Fig. 16, the lines of the PDF are not shown when the probability is zero, e.g., $[\varepsilon_\varphi]_\mathrm{V} \lesssim 10^{-5}$ and $10^{-2} \lesssim [\varepsilon_\varphi]_\mathrm{V}$. The PDF of the instantaneous scalar dissipation rate ε_φ in the DNS is also shown for comparison. It is known that ε_φ is highly intermittent in space, and the PDF indicates that ε_φ ranges between 10^{-7} and 10^{-1}. Once the volume average is applied to calculate $[\varepsilon_\varphi]_\mathrm{V}$, these regions with extremely large and small ε_φ are averaged, and the PDF of $[\varepsilon_\varphi]_\mathrm{V}$ has non-zero values in a narrower range than that of ε_φ. The PDF of $[\varepsilon_\varphi]_\mathrm{V}$ indicates that $[\varepsilon_\varphi]_\mathrm{V}$ has values within the range of $10^{-5} \lesssim [\varepsilon_\varphi]_\mathrm{V} \lesssim 10^{-2}$ in both DNS and Lagrangian simulation. Thus, the level of fluctuations in $[\varepsilon_\varphi]_\mathrm{V}$ is also well predicted by the model used in Lagrangian simulation.

6. Conclusion

We assessed the performance of two models developed for molecular diffusion in Lagrangian simulation coupled with LES used for turbulent mixing in compressible turbulence, where the filtered Navier–Stokes equations are solved with LES while advective-diffusive scalars are simulated with the computational particles in Lagrangian simulation. One of the models evaluated in this study was the mixing volume model (MVM) for the molecular diffusion. Another one was the model for the coarse-grained scalar dissipation rate, which appears as an unknown quantity in the MVM. Here, coarse-grained quantities in Lagrangian simulation are defined with the ensemble averages

of the mixing particles within the mixing volume. The particle-based model was developed from the SGS model for the filtered scalar dissipation rate, which was originally developed for LES of compressible flows. The model for the coarse-grained dissipation rate was evaluated with a priori test based on the DNS database of the temporally evolving turbulent planar jet with subsonic or supersonic jet velocity. It was shown that the coarse-grained scalar dissipation rate is well estimated by the present model based on particles, and the model is independent of the size of the volume that defines the coarse-grained quantities when the number of the mixing particles used in the model is about 10-14. The model tends to overestimate the coarse-grained scalar dissipation rate in regions with strong dilatation fluctuations. However, even in the supersonic jet, most flow regions have weak dilatation fluctuations, and the average of the coarse-grained scalar dissipation rate is still well estimated by the present model.

The MVM and the particle model of the coarse-grained scalar dissipation rate were implemented in LES and Lagrangian simulation of compressible flows. It should be noted that these models have been used only in numerical simulations for incompressible flows in previous studies.[14,24] Lagrangian simulation coupled with LES with these models was conducted for passive scalar mixing of the subsonic or supersonic temporally evolving planar jet, for which the DNS database is available for comparison. Lagrangian simulation accurately predicted the mean and rms scalar fluctuations of passive scalar and the turbulent scalar flux. The statistics of the coarse-grained scalar dissipation rate obtained by the model in Lagrangian simulation also agreed well with the DNS results, and the model accurately calculated the instantaneous

coarse-grained dissipation rate in the context of Lagrangian simulation. As the statistics obtained in Lagrangian simulation hardly change with the total number of particles, no computational parameters need to be adjusted for the models for the molecular diffusion. The present results suggested that LES/Lagrangian simulation with the MVM combined with the particle-based dissipation model is a promising tool for future study on numerical simulations of high-speed reacting flows as Lagrangian simulation does not require the models for the SGS chemical source terms.

Acknowledgment

The numerical simulations presented in this manuscript were carried out on the high-performance computing system (NEC SX-ACE) in the Japan Agency for Marine-Earth Science and Technology. This work was partially supported by "Collaborative Research Project on Computer Science with High-Performance Computing in Nagoya University" and by JSPS KAKENHI Grant Number 18H01367.

[1] P. K. Senecal, E. Pomraning, K. J. Richards, S. Som, Grid-convergent spray models for internal combustion engine CFD simulations, in: ICEF2012, ASME Digital Collection, 2012, pp. 697–710.

[2] M. Raju, M. Wang, M. Dai, W. Piggott, D. Flowers, Acceleration of detailed chemical kinetics using multi-zone modeling for CFD in internal combustion engine simulations, Tech. Rep. 2012-01-0135, SAE Technical Paper (2012).

[3] S. Mauro, R. Sener, M. Z. Gul, R. Lanzafame, M. Messina, S. Brusca, Internal combustion engine heat release calculation using single-zone and CFD 3D numerical models, Int. J. Energy Environ. Eng. 9 (2) (2018) 215–226.

[4] U. Schumann, Large-eddy simulation of turbulent diffusion with chemical reactions in the convective boundary layer, Atmos. Environ. 23 (8) (1989) 1713–1727.

[5] T. Michioka, S. Komori, Large-eddy simulation of a turbulent reacting liquid flow, AIChE J. 50 (11) (2004) 2705–2720.

[6] A. Y. Klimenko, R. W. Bilger, Conditional moment closure for turbulent combustion, Prog. Energy Combust. Sci. 25 (6) (1999) 595–687.

[7] P. J. Colucci, F. A. Jaberi, P. Givi, S. B. Pope, Filtered density function for large eddy simulation of turbulent reacting flows, Phys. Fluids 10 (1998) 499.

[8] D. H. Rowinski, S. B. Pope, Computational study of lean premixed turbulent flames using RANSPDF and LESPDF methods, Combust. Theory Model. 17 (4) (2013) 610–656.

[9] W. Han, V. Raman, Z. Chen, LES/PDF modeling of autoignition in a lifted turbulent flame: Analysis of flame sensitivity to differential diffusion and scalar mixing time-scale, Combust. Flame 171 (2016) 69–86.

[10] M. R. H. Sheikhi, T. G. Drozda, P. Givi, F. A. Jaberi, S. B. Pope, Large eddy simulation of a turbulent nonpremixed piloted methane jet flame (Sandia Flame D), Proc. Combust. Inst. 30 (1) (2005) 549–556.

[11] A. Banaeizadeh, Z. Li, F. A. Jaberi, Compressible scalar filtered mass density function model for high-speed turbulent flows, AIAA J. 49 (10) (2011) 2130–2143.

[12] Z. Huang, M. J. Cleary, H. Zhang, Application of the sparse-Lagrangian multiple mapping conditioning approach to a model supersonic combustor, Physics of Fluids 32 (10) (2020) 105120.

[13] C. Le Ribault, S. Simoens, I. Vinkovic, Hybrid large eddy simulation/Lagrangian stochastic model for turbulent passive and reactive scalar dispersion in a plane jet, Chem. Eng. Commun. 199 (4) (2012) 435–460.

[14] T. Watanabe, Y. Sakai, K. Nagata, Y. Ito, T. Hayase, LES–lagrangian particle method for turbulent reactive flows based on the approximate deconvolution model and mixing model, J. Comput. Phys. 294 (2015) 127–148.

[15] S. B. Pope, PDF methods for turbulent reactive flows, Prog. Energy Combust. Sci. 11 (2) (1985) 119–192.

[16] R. O. Fox, Computational Models for Turbulent Reacting Flows, Cambridge Univ. Pr., 2003.

[17] J. Villermaux, J. C. Devillon, Representation of the coalescence and the redispersion of the fields of segregation in a fluid by a model of phenomenologic interaction, Chemical Reaction Engineering: Proceedings of the Fifth European/Second International Symposium on Chemical Reaction Engineering (1972) B1–13.

[18] T. Watanabe, K. Nagata, Mixing model with multi-particle interactions for Lagrangian simulations of turbulent mixing, Phys. Fluids 28 (8) (2016) 085103.

[19] I. Vinkovic, C. Aguirre, S. Simoens, Large-eddy simulation and Lagrangian stochastic modeling of passive scalar dispersion in a turbulent boundary layer, J. Turbulence (7) (2006) N30.

[20] C. D. Pierce, P. Moin, A dynamic model for subgrid-scale variance and dissipation rate of a conserved scalar, Phys. Fluids 10 (1998) 3041.

[21] A. W. Cook, W. K. Bushe, A subgrid-scale model for the scalar dissipation rate in nonpremixed combustion, Phys. Fluids 11 (3) (1999) 746–748.

[22] C. Jimenez, F. Ducros, B. Cuenot, B. Bedat, Subgrid scale variance and dissipation of a scalar field in large eddy simulations, Phys. Fluids 13 (6) (2001) 1748–1754.

[23] Y. Ge, M. J. Cleary, A. Y. Klimenko, Sparse-Lagrangian FDF simulations of Sandia Flame E with density coupling, Proc. Combust. Inst. 33 (1) (2011) 1401–1409.

[24] S. Tanaka, T. Watanabe, K. Nagata, Multi-particle model of coarse-grained scalar dissipation rate with volumetric tensor in turbulence, J. Comput. Phys. 389 (2019) 128–146.

[25] T. Watanabe, K. Nagata, LES–lagrangian-particles-simulation of turbulent reactive flows at high Sc number using approximate deconvolution model, AIChE Journal 62 (8) (2016) 2912–2922.

[26] Y. Tai, T. Watanabe, K. Nagata, Modeling of molecular diffusion and thermal conduction with multi-particle interaction in compressible turbulence, Phys. Fluids 30 (3) (2018) 035108.

[27] J. P. Boris, On Large Eddy simulation using subgrid turbulence models comment 1, In: Whither turbulence? Turbulence at the crossroads (1990) 344–353.

[28] S. B. Pope, Simple models of turbulent flows, Phys. Fluids 23 (1) (2011) 011301.

[29] V. Raman, H. Pitsch, R. O. Fox, Hybrid large-eddy simulation/Lagrangian filtered-density-function approach for simulating turbulent combustion, Combust. Flame 143 (1-2) (2005) 56–78.

[30] V. Raman, H. Pitsch, A consistent LES/filtered-density function formulation for the simulation of turbulent flames with detailed chemistry, Proc. Combust. Inst. 31 (2) (2007) 1711–1719.

[31] P. A. Davidson, Turbulence: an introduction for scientists and engineers, Oxford university press, 2015.

[32] A. Y. Klimenko, Lagrangian particles with mixing. II. Sparse-Lagrangian methods in application for turbulent reacting flows, Phys. Fluids 21 (6) (2009) 065102.

[33] P. Robert, A. Roux, C. C. Harvey, M. W. Dunlop, P. W. Daly, K. H. Glassmeier, Tetrahedron geometric factors, Analysis Methods for Multi-Spacecraft Data (1998) 323–348.

[34] T. Watanabe, K. Nagata, Gradients estimation from random points with volumetric tensor in turbulence, J. Comput. Phys. 350 (2017) 518–529.

[35] R. Nagata, T. Watanabe, K. Nagata, Turbulent/non-turbulent interfaces in temporally evolving compressible planar jets, Phys. Fluids 30 (10) (2018) 105109.

[36] C. B. da Silva, J. C. F. Pereira, Invariants of the velocity-gradient, rate-of-strain, and rate-of-rotation tensors across the turbulent/nonturbulent interface in jets, Phys. Fluids 20 (5) (2008) 055101.

[37] R. Jahanbakhshi, C. K. Madnia, Entrainment in a compressible turbulent shear layer, J. Fluid Mech. 797 (2016) 564–603.

[38] M. Gampert, J. Boschung, F. Hennig, M. Gauding, N. Peters, The vorticity versus the scalar criterion for the detection of the turbulent/non-turbulent interface, J. Fluid Mech. 750 (2014) 578–596.

[39] M. van Reeuwijk, M. Holzner, The turbulence boundary of a temporal jet, J. Fluid Mech. 739 (2014) 254–275.

[40] J. Berland, C. Bogey, C. Bailly, Numerical study of screech generation in a planar supersonic jet, Phys. Fluids 19 (7) (2007) 075105.

[41] A. Kempf, M. Klein, J. Janicka, Efficient generation of initial-and inflow-conditions for transient turbulent flows in arbitrary geometries, Flow Turbul. Combust. 74 (1) (2005) 67–84.

[42] P. K. Yeung, S. B. Pope, An algorithm for tracking fluid particles in

numerical simulations of homogeneous turbulence, J. Comput. Phys. 79 (2) (1988) 373–416.

[43] S. B. Pope, Turbulent flows (2001).

[44] G. Sardina, F. Picano, P. Schlatter, L. Brandt, C. M. Casciola, Large scale accumulation patterns of inertial particles in wall-bounded turbulent flow, Flow Turbul Combust. 86 (3-4) (2011) 519–532.

[45] T. Watanabe, C. B. da Silva, K. Nagata, Multi-particle dispersion during entrainment in turbulent free-shear flows, J. Fluid Mech. 805.

[46] Q. Ni, Compressible turbulent mixing: Effects of compressibility, Phys. Rev. E 93 (4) (2016) 043116.

[47] A. D. Chorny, Comparison of micromixing models for calculation of the chemical reaction rate in homogeneous turbulent flow, Chem. Eng. Technol. 32 (12) (2009) 1866–1874.

[48] D. W. Meyer, R. Deb, Modeling molecular mixing in a spatially inhomogeneous turbulent flow, Phy. Fluids 24 (2) (2012) 025103.

[49] D. W. Meyer, P. Jenny, Accurate and computationally efficient mixing models for the simulation of turbulent mixing with PDF methods, J. Comput. Phys. 247 (2013) 192–207.

[50] X. Zhang, T. Watanabe, K. Nagata, Turbulent/nonturbulent interfaces in high-resolution direct numerical simulation of temporally evolving compressible turbulent boundary layers, Phys. Rev. Fluids 3 (9) (2018) 094605.

[51] G. Lodato, P. Domingo, L. Vervisch, Three-dimensional boundary conditions for direct and Large-Eddy simulation of compressible viscous flows, J. Comput. Phys 227 (10) (2008) 5105–5143.

[52] Z. Wang, Y. Lv, P. He, J. Zhou, K. Cen, Fully explicit implementation of direct numerical simulation for a transient near-field methane/air diffusion jet flame, Comput. Fluids 39 (8) (2010) 1381–1389.

[53] C. Bogey, C. Bailly, A family of low dispersive and low dissipative explicit schemes for flow and noise computations, J. Comput. Phys. 194 (1) (2004) 194–214.

[54] C. A. Kennedy, M. H. Carpenter, Several new numerical methods for compressible shear-layer simulations, Appl. Numer. Math. 14 (4) (1994) 397–433.

[55] C. Bogey, N. De Cacqueray, C. Bailly, A shock-capturing methodology based on adaptative spatial filtering for high-order non-linear computations, J. Comput. Phys. 228 (5) (2009) 1447–1465.

[56] Y. Tai, T. Watanabe, K. Nagata, Implicit large eddy simulation of passive scalar transfer in compressible planar jet, Int. J. Numer. Meth. Fluids.

[57] Z. Wang, P. He, Y. Lv, J. Zhou, J. Fan, K. Cen, Direct numerical simulation of subsonic round turbulent jet, Flow Turbul. Combust. 84 (4) (2010) 669–686.

[58] C. B. da Silva, O. Métais, On the influence of coherent structures upon

interscale interactions in turbulent plane jets, J. Fluid Mech. 473 (2002) 103–145.

[59] D. W. Bogdanoff, Compressibility effects in turbulent shear layers, AIAA J. 21 (6) (1983) 926–927.

[60] S. Stanley, S. Sarkar, J. Mellado, A study of the flow-field evolution and mixing in a planar turbulent jet using direct numerical simulation, J. Fluid Mech. 450 (2002) 377–407.

[61] R. A. Antonia, L. W. B. Browne, S. Rajagopalan, A. J. Chambers, On the organized motion of a turbulent plane jet, J. Fluid Mech. 134 (1983) 49–66.

[62] O. Terashima, Y. Sakai, K. Nagata, Simultaneous measurement of all three velocity components and pressure in a plane jet, Meas. Sci. Technol. 25 (5) (2014) 055301.

[63] R. Jahanbakhshi, C. K. Madnia, Viscous superlayer in a reacting compressible turbulent mixing layer, J. Fluid Mech. 848 (2018) 743–755.

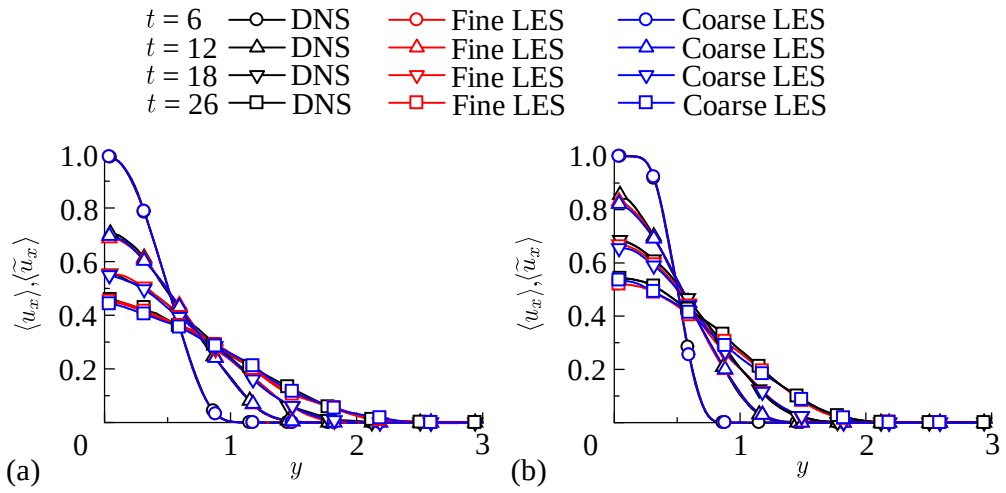

Figure 6: Lateral profiles of mean streamwise velocity in the planar jet with (a) $M_{\mathrm{J}} = 0.6$ and (b) $M_{\mathrm{J}} = 1.6$ in LES with $(N_x, N_y, N_z) = (480, 300, 240)$ (fine LES) and $(360, 300, 180)$ (coarse LES). DNS results[26] are also shown for comparison.

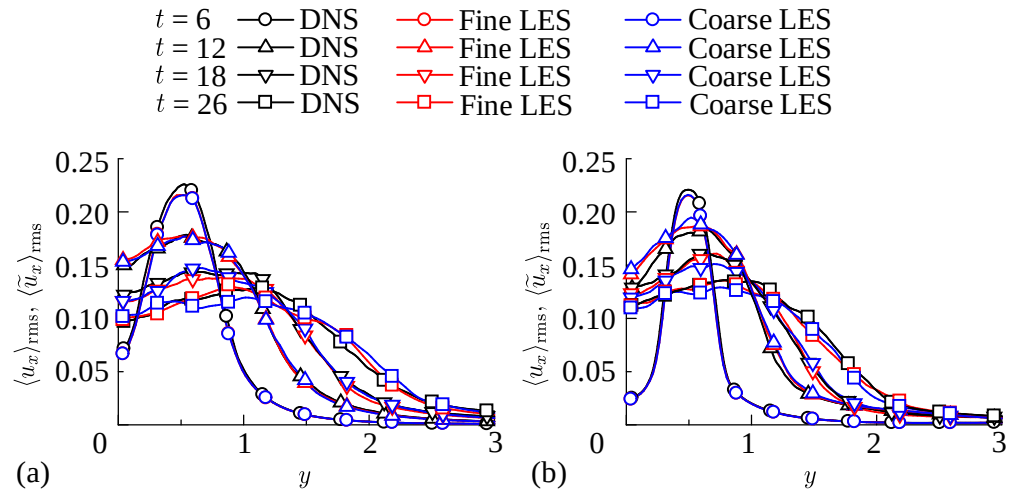

Figure 7: Lateral profiles of rms fluctuations of streamwise velocity in the planar jet with (a) $M_\mathrm{J} = 0.6$ and (b) $M_\mathrm{J} = 1.6$ in LES with $(N_x, N_y, N_z) = (480, 300, 240)$ (fine LES) and $(360, 300, 180)$ (coarse LES). DNS results[26] are also shown for comparison.

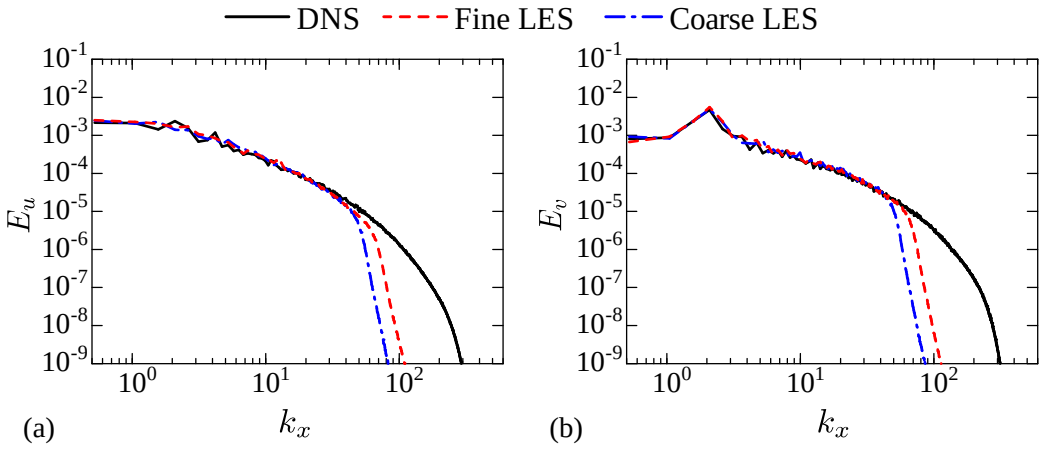

Figure 8: Energy spectra of (a) streamwise velocity and (b) lateral velocity on the jet centerline at $t = 12$ in LES with $(N_x, N_y, N_z) = (480, 300, 240)$ (fine LES) and $(360, 300, 180)$ (coarse LES). DNS results[26] are also shown for comparison.

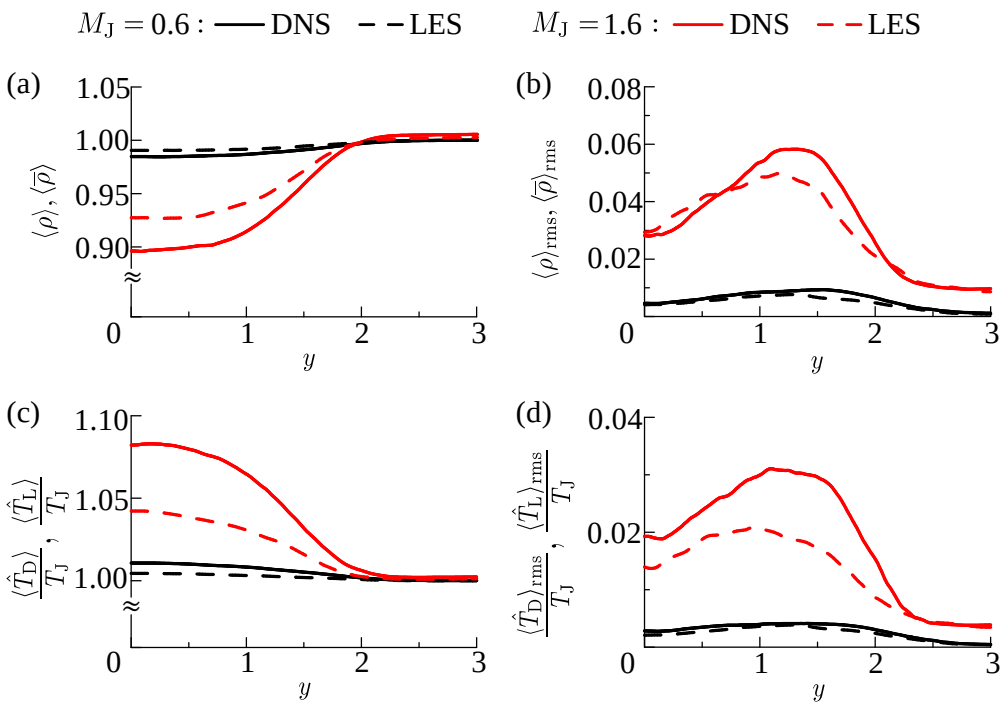

Figure 9: Comparison between LES with $(N_x, N_y, N_z) = (480, 300, 240)$ and DNS at $t = 26$. Lateral profiles of (a) mean density, (b) rms density fluctuations, (c) mean temperature, and (d) rms temperature fluctuations.

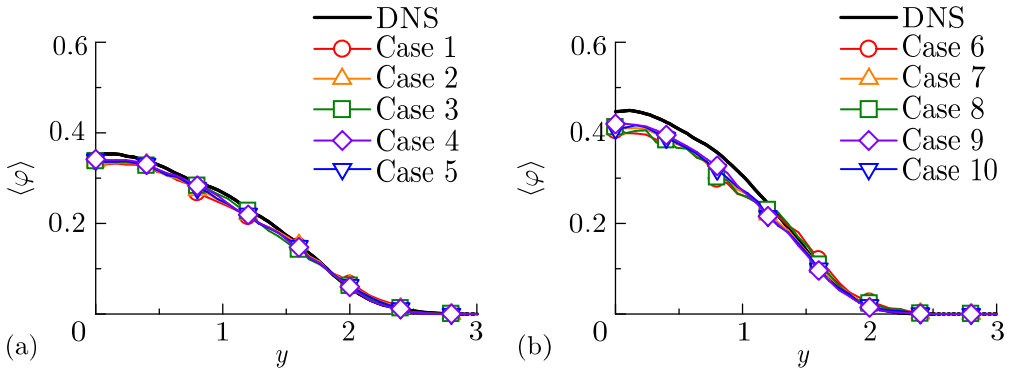

Figure 10: Mean scalar profiles at $t = 26$ for (a) $M_{\mathrm{J}} = 0.6$ and (b) $M_{\mathrm{J}} = 1.6$.

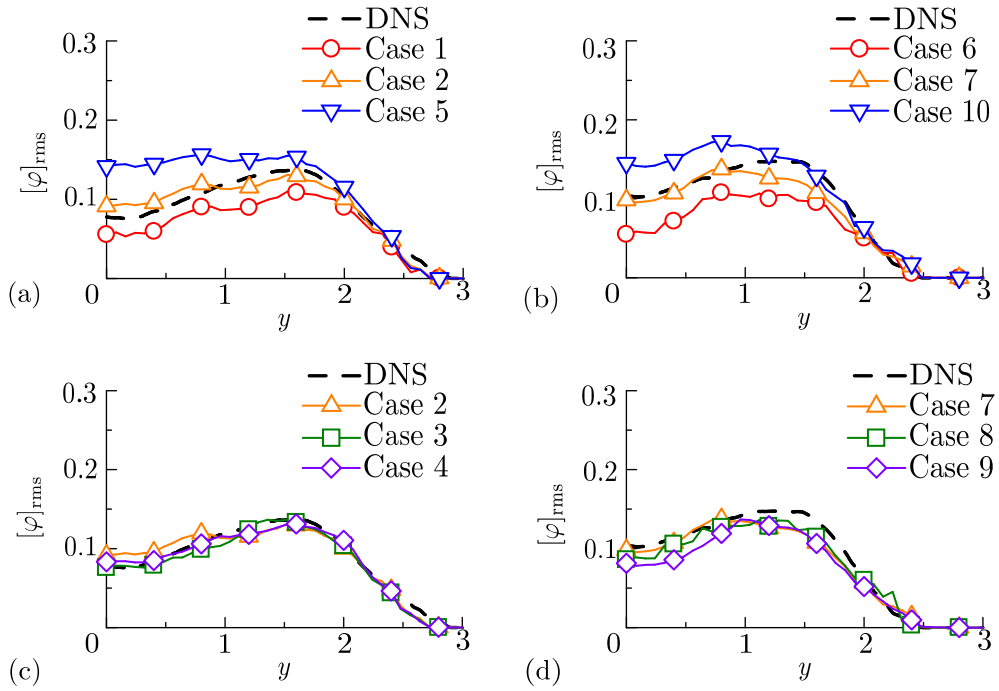

Figure 11: Lateral profiles of rms scalar fluctuations in DNS and Lagrangian simulation: (a) cases 1, 2, and 5 ($M_{\rm J} = 0.6$) with $R_{\rm MV} = 120\eta$; (b) cases 6, 7, and 10 ($M_{\rm J} = 0.6$) with $N_{\rm M} = 12$; (c) cases 2, 3, and 4 ($M_{\rm J} = 1.6$) with $R_{\rm MV} = 110\eta$; (d) cases 7, 8, and 9 ($M_{\rm J} = 1.6$) with $N_{\rm M} = 12$.

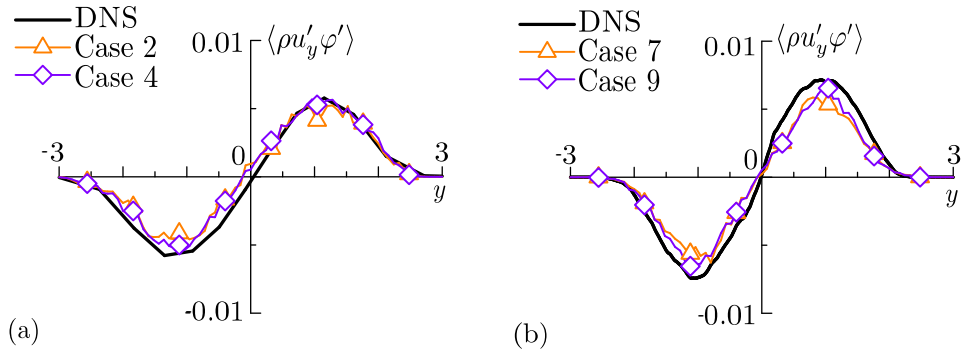

Figure 12: Lateral profiles of turbulent scalar flux $\langle \rho u_y' \varphi' \rangle$ at $t = 26$.

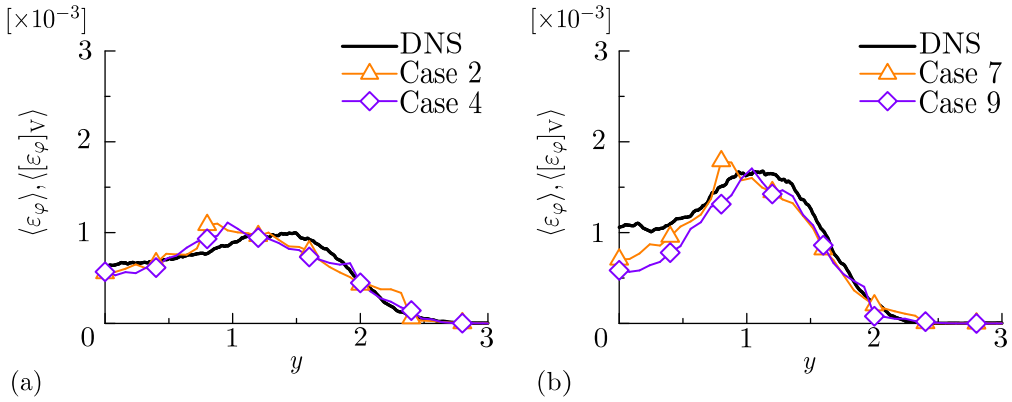

Figure 13: Lateral profiles of mean coarse-grained scalar dissipation rate $\langle [\varepsilon_\varphi]_V \rangle$ in Lagrangian simulation and mean scalar dissipation rate $\langle \varepsilon_\varphi \rangle$ in DNS at (a) $M_J = 0.6$ and (b) $M_J = 1.6$ ($t = 26$).

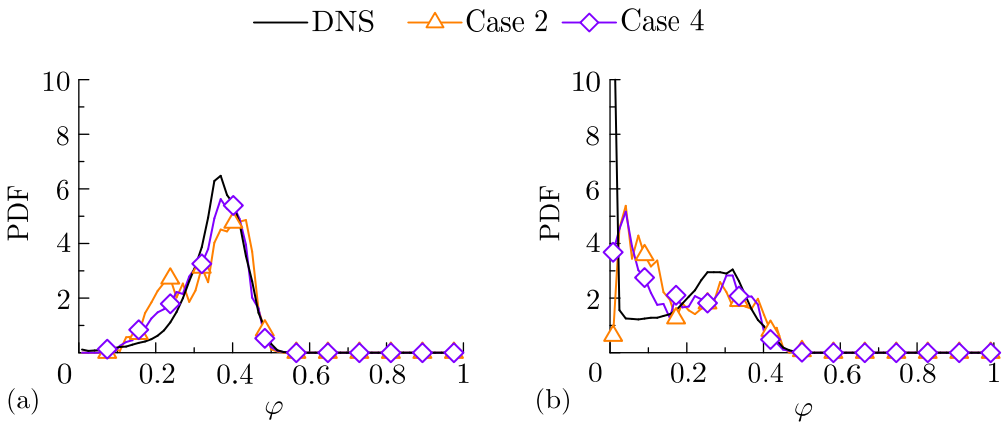

Figure 14: Probability density functions of φ in DNS and Lagrangian simulation at (a) $y = 0$ and (b) $y = b_\varphi$ for $M_\mathrm{J} = 0.6$.

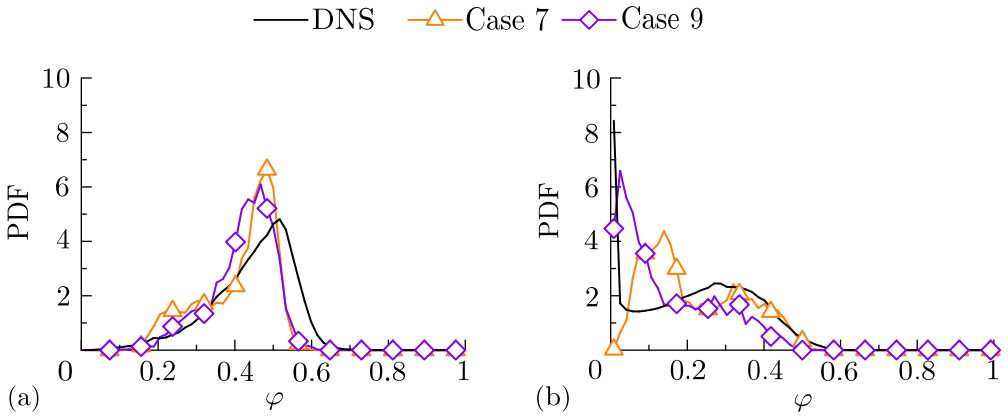

Figure 15: Probability density functions of φ in DNS and Lagrangian simulation at (a) $y = 0$ and (b) $y = b_\varphi$ for $M_\mathrm{J} = 1.6$.

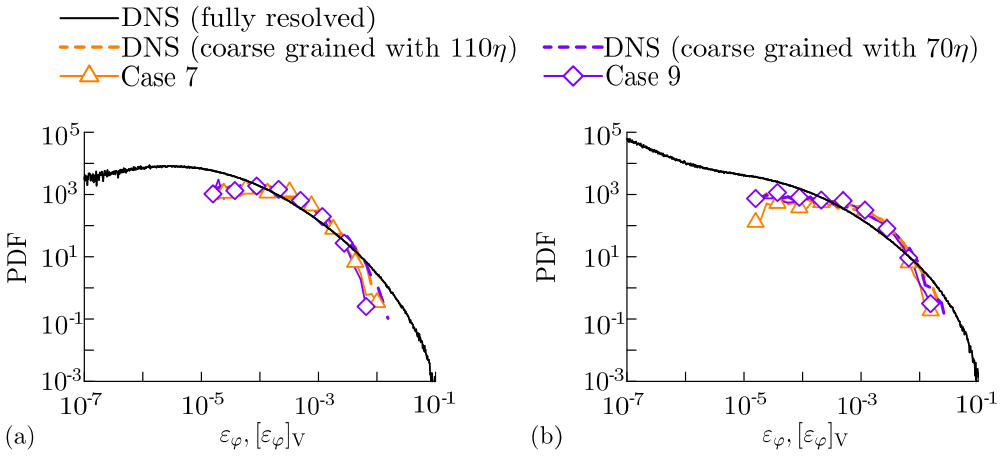

Figure 16: Probability density functions of fully-resolved scalar dissipation rate ε_φ and coarse-grained scalar dissipation rate $[\varepsilon_\varphi]_\mathrm{V}$ at (a) $y = 0$ and (b) $y = b_\varphi$. The results are taken at $t = 26$ from the simulations for $M_\mathrm{J} = 1.6$.